




Blood Lipoproteins Shape the Phenotype and Lipid Content of Early Atherosclerotic Lesion Macrophages: A Dual-Structured Mathematical Model

Keith L. Chambers¹  · Mary R. Myerscough² · Michael G. Watson³ · Helen M. Byrne^{1,4}

Received: 10 April 2024 / Accepted: 16 July 2024
© The Author(s) 2024

Abstract

Macrophages in atherosclerotic lesions exhibit a spectrum of behaviours or *phenotypes*. The phenotypic distribution of monocyte-derived macrophages (MDMs), its correlation with MDM lipid content, and relation to blood lipoprotein densities are not well understood. Of particular interest is the balance between low density lipoproteins (LDL) and high density lipoproteins (HDL), which carry *bad* and *good* cholesterol respectively. To address these issues, we have developed a mathematical model for early atherosclerosis in which the MDM population is structured by phenotype and lipid content. The model admits a simpler, closed subsystem whose analysis shows how lesion composition becomes more pathological as the blood density of LDL increases relative to the HDL capacity. We use asymptotic analysis to derive a power-law relationship between MDM phenotype and lipid content at steady-state. This relationship enables us to understand why, for example, lipid-laden MDMs have a more inflammatory phenotype than lipid-poor MDMs when blood LDL lipid density

✉ Keith L. Chambers
keith.chambers@maths.ox.ac.uk

Mary R. Myerscough
mary.myerscough@sydney.edu.au

Michael G. Watson
michael.watson1@unsw.edu.au

Helen M. Byrne
helen.byrne@maths.ox.ac.uk

- ¹ Wolfson Centre for Mathematical Biology, Mathematical Institute, University of Oxford, Andrew Wiles Building, Radcliffe Observatory Quarter, Woodstock Road, Oxford, Oxfordshire OX2 6GG, UK
- ² School of Mathematics and Statistics, University of Sydney, Carlaw Building, Eastern Avenue, Camperdown, Sydney, NSW 2006, Australia
- ³ School of Mathematics and Statistics, University of New South Wales, Anita B. Lawrence Centre, University Mall, UNSW, Kensington, Sydney, NSW 2052, Australia
- ⁴ Ludwig Institute for Cancer Research, University of Oxford, Old Road Campus Research Build, Roosevelt Dr, Headington, Oxford, Oxfordshire OX3 7DQ, UK

greatly exceeds HDL capacity. We show further that the MDM phenotype distribution always attains a local maximum, while the lipid content distribution may be unimodal, adopt a quasi-uniform profile or decrease monotonically. Pathological lesions exhibit a local maximum in both the phenotype and lipid content MDM distributions, with the maximum at an inflammatory phenotype and near the lipid content capacity respectively. These results illustrate how macrophage heterogeneity arises in early atherosclerosis and provide a framework for future model validation through comparison with single-cell RNA sequencing data.

Keywords Phenotype · Lipid · Structured population model · Atherosclerosis · Discrete · Continuum

1 Introduction

Atherosclerosis is a chronic inflammatory condition of the artery wall (Bäck et al. 2019). The disease begins with the retention of low-density-lipoprotein (LDL) particles in the artery wall. LDL particles, which carry fatty compounds called lipids, enter the artery wall from the bloodstream and are retained via interactions with extracellular matrix. Retained LDL (rLDL) particles are rapidly modified via oxidation and aggregation. The accumulation of rLDL particles triggers an immune response that attracts monocyte-derived macrophages (MDMs) to the lesion. MDMs are typically the most numerous immune cell type in early atherosclerotic lesions (Willemsen and de Winther 2020). They play a key role in disease progression by ingesting extracellular lipid and offloading lipid to high-density lipoprotein (HDL) particles, which also enter the lesion from the bloodstream (Kloc et al. 2020). Importantly, MDMs may adopt a variety of phenotypes depending on their interaction with the lesion microenvironment (Tabas and Bornfeldt 2016; Bäck et al. 2019). This includes inflammatory (M1-like) and resolving (M2-like) phenotypes. Over time, sustained inflammation and the death of lipid-laden MDMs may cause the lesion to transition into an atherosclerotic plaque with a large core of extracellular lipid (Guyton and Klemp 1996; Gonzalez and Trigatti 2017). The rupture of this plaque releases the lipid core into the bloodstream, where it promotes blood clot formation and can induce an acute clinical event. Plaque rupture is the most common cause of myocardial infarction (Costopoulos et al. 2017) and a leading cause of ischaemic strokes (Rothwell 2007). Understanding how the *in vivo* distribution of MDM phenotype is influenced by MDM lipid content and blood LDL/HDL densities are active areas of research.

Macrophages in atherosclerotic lesions exhibit a continuum of inflammatory to resolving phenotypes (Leitinger and Schulman 2013; Bäck et al. 2019). This view supersedes the traditional dichotomous M1/M2 classification of macrophage phenotype; M1 and M2 polarisation now typically refer to the extremes of a phenotype continuum (Barrett 2020). Macrophage phenotype modulation appears to be reversible (Barrett 2020; Lin et al. 2021; Wang et al. 2014), and is largely determined by the balance between (pro-)inflammatory and (pro-)resolving mediators (Tabas and Bornfeldt 2016; Bäck et al. 2019). Following the classification presented in Tabas and Bornfeldt (2016), inflammatory mediators include cytokines such as TNF and IL-1,

that are secreted by MDMs upon uptake of modLDL (Liu et al. 2014), and damage associated molecular patterns (DAMPs) that are released upon the secondary necrosis of apoptotic cells (Sachet et al. 2017). Resolving mediators include the cytokines IL-10 and IL-13, and specialised pro-resolving lipid mediators. Resolving mediators are synthesised by macrophages upon apoptotic cell uptake (Decker et al. 2021) and interaction with HDL (Serhan and Levy 2018). LDL and HDL promote the synthesis of opposing mediator types (inflammatory and resolving respectively) and, so, are likely to induce opposing effects on MDM phenotype.

Mathematical models of atherosclerosis are an emerging field of study (Parton et al. 2016; Avgerinos and Neofytou 2019; Cai and Li 2021; Mc Auley 2022). The existing literature includes (i) models of LDL infiltration (Prosi et al. 2005; Yang and Vafai 2006, 2008), (ii) mechanical models of plaque growth (Fok 2012; Watson et al. 2018; Fok and Lanzer 2018; Watson et al. 2020; Fok and Mirzaei 2021), and (iii) models that focus on lesion immunology. Lesion immunology has been modelled using ODEs (Bulelzai and Dubbeldam 2012; Cohen et al. 2014; Islam and Johnston 2015; Thon et al. 2018; Lui and Myerscough 2021; Xie 2022), spatial PDEs (Calvez et al. 2009; Fok 2012; Hao and Friedman 2014; Chalmers et al. 2015; Mukherjee et al. 2019; Mohammad Mirzaei et al. 2020; Ahmed et al. 2023) and agent-based approaches (Corti et al. 2020; Bayani et al. 2020). Importantly, existing models which incorporate macrophage phenotype do so via binary M1/M2 classification rather than a continuum setting (Friedman and Hao 2015; Bezyaev et al. 2020; Liu et al. 2022). Macrophage lipid content is also typically treated via a binary distinction between macrophages with little internalised lipid (simply termed ‘macrophages’) and those that are lipid-laden (termed ‘foam cells’) (Calvez et al. 2009; Hao and Friedman 2014; Chalmers et al. 2017; Silva et al. 2020). However, several recent studies capture gradual lipid accumulation in lesion macrophages via structured population modelling (Ford et al. 2019; Meunier and Muller 2019; Chambers et al. 2022, 2023; Watson et al. 2023).

Of particular relevance is the recent lipid-structured model of Chambers et al. (2023), which serves as the foundation of the present study. By extending this model to account for simultaneous variation in MDM phenotype *and* lipid content, we provide a mechanistic framework to explore the diversity of lipid-associated macrophage states revealed by single-cell RNA sequencing (Dib et al. 2023). Other authors have proposed dual-structured mathematical models (e.g. Bernard et al. 2003; Doumic 2007; Laroche and Perasso 2016; Hodgkinson et al. 2019, reviewed in Kang et al. (2020)). A key difference between these existing models and ours relates to the time evolution of the structure variables: in most existing models, the structure variables are independent whereas in our model their time evolution is coupled. We use our dual-structured model to address the following questions:

1. *How do blood LDL/HDL levels impact lesion composition?*
 - a. How do they affect the time-evolution of lesion composition?
 - b. How do they affect lesion composition at steady state?
2. *How are phenotype and lipid content distributed among MDMs?*
 - a. How do MDM phenotype and lipid content evolve over time?
 - b. Are MDM phenotype and lipid content correlated?

- c. What are the qualitative features of the phenotype and lipid content marginal distributions at steady state?

The remainder of the paper is structured as follows. Sect. 2 details the model development, including the derivation of a closed subsystem and discussion of parameter values. Sect. 3 contains the results of our model analysis. Key questions 1 and 2 are addressed in Sects. 3.1 and 3.2, respectively. Finally, we discuss the results and their implications in Sect. 4.

2 Model Development

In this section we present a phenotype-lipid dual-structured model for MDM populations in early atherosclerosis. Model schematics for the MDM dynamics and LDL retention are given in Figs. 1 and 2, respectively.

2.1 Assumptions and Definitions

We assume for simplicity that macrophage phenotype and lipid content change by finite increments, $\Delta\phi = 1$ and $\Delta a > 0$ respectively. Specifically, we let $m_{\phi,\ell}(t)$ denote the number density of MDMs with phenotype ϕ and lipid content $a_0 + \ell\Delta a$ at time $t \geq 0$. The phenotype index runs over both positive and negative integer values: $\phi = 0, \pm 1, \dots, \pm\phi_{\max}$. Macrophages with $\phi > 0$ are pro-inflammatory and have an M1-like phenotype; those with $\phi < 0$ are anti-inflammatory and have an M2-like phenotype. The extreme values $\phi = \pm\phi_{\max}$ can be interpreted as complete M1 and M2 polarisation. The lipid index runs over non-negative values: $\ell = 0, 1, \dots, \ell_{\max}$, so that macrophage lipid content ranges from their endogenous content, $a_0 \geq 0$, to a maximum value, $a_0 + \kappa$, where $\kappa := \ell_{\max}\Delta a$ is the maximum capacity for ingested lipid.

We also introduce variables to describe the extracellular environment. We denote by $L_{LDL}(t) \geq 0$, $L_r(t) \geq 0$, $L_{ap}(t) \geq 0$ and $L_n(t) \geq 0$ the mass densities of free LDL lipid, retained LDL lipid, apoptotic lipid and necrotic lipid respectively. We let $H(t)$ be the lipid capacity of HDL particles in the lesion. Finally, we denote by $S_+(t) \geq 0$ and $S_-(t) \geq 0$ the mass densities of inflammatory and resolving mediators respectively.

We note that all dependent variables in the model denote densities within the *tunica intima*. This is the innermost region of the artery wall where atherosclerosis develops (Bäck et al. 2019). As shown in Figs. 1 and 2, the intimal densities are nonetheless affected by the bloodstream and *tunica media* (the next layer of the artery wall) via the flux of cells and lipids. We assume for simplicity that the contents of the bloodstream and *tunica media* are static in the equations below.

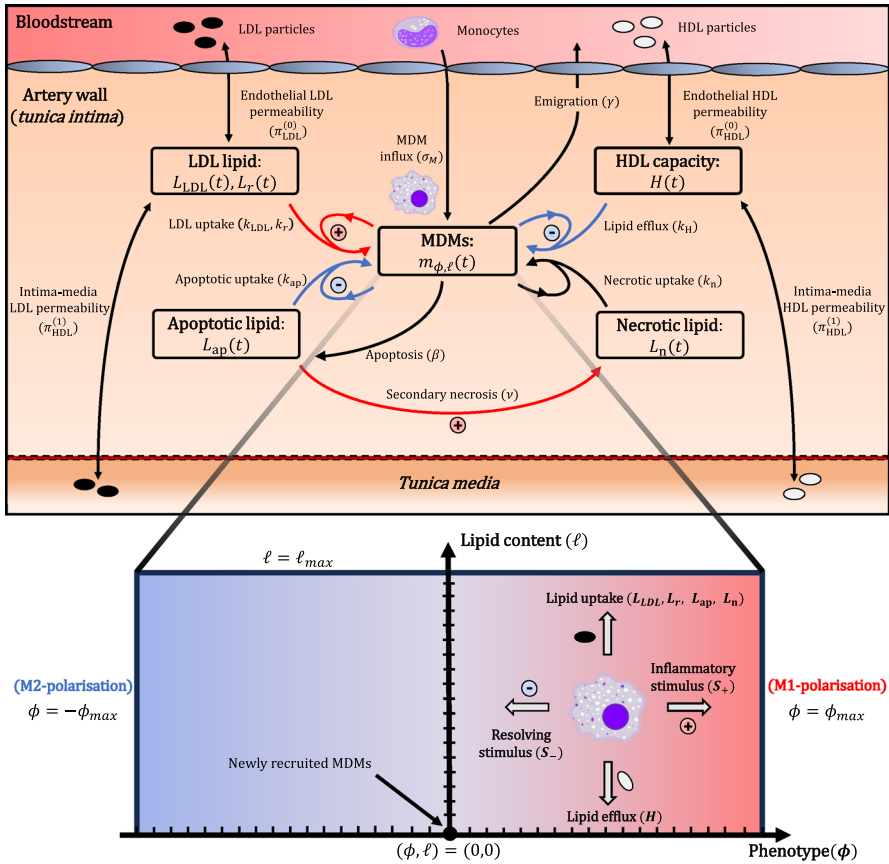


Fig. 1 A schematic of the MDM-lipid dynamics in the model. Processes represented with blue arrows stimulate the secretion of resolving mediators by MDMs, while those represented by red arrow stimulate the emission of inflammatory mediators. The lower half illustrates the discrete phenotype-lipid structure space that underpins the MDM dynamics. LDL retention and constitutive mediator production by MDMs are not shown

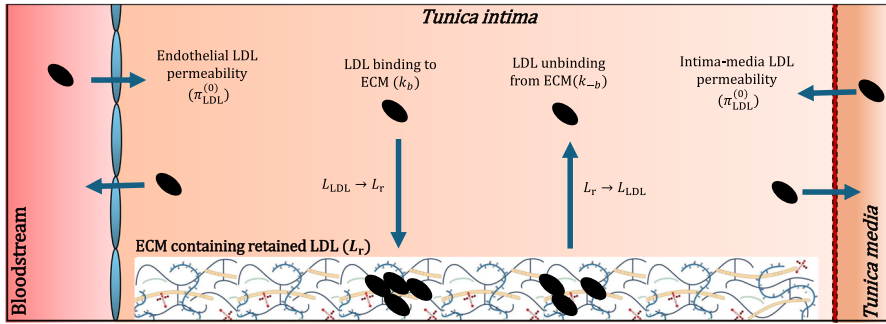


Fig. 2 Schematic of the LDL kinetics in absence of MDMs. The model distinguishes between free LDL (L_{LDL}), which diffuses freely between the bloodstream, tunica intima and tunica media, and retained LDL (L_r) that is bound to the ECM within the tunica intima. We assume in Eqs. (7)–(8) that the ECM has a finite capacity for rLDL, K_r , and that the rate of binding is proportional to the available capacity: $k_b(K_r - L_r)$

2.2 Model Equations

MDMs. We propose that the MDM population evolves according to the following ODEs:

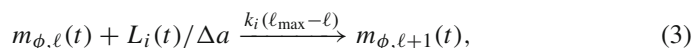
$$\begin{aligned}
 \frac{d}{dt}m_{\phi,\ell} = & \underbrace{k_L \cdot L [(\ell_{\max} - \ell + 1)m_{\phi,\ell-1} - (\ell_{\max} - \ell)m_{\phi,\ell}]}_{\text{lipid uptake}} \\
 & + \underbrace{k_H H [(\ell + 1)m_{\phi,\ell+1} - \ell m_{\phi,\ell}]}_{\text{lipid efflux to HDL}} \\
 & + \underbrace{k_S \chi S_+ [(\phi_{\max} - \phi + 1)m_{\phi+1,\ell} - (\phi_{\max} - \phi)m_{\phi,\ell}]}_{\text{inflammatory phenotype modulation}} \\
 & + \underbrace{k_S \chi S_- [(\phi_{\max} + \phi + 1)m_{\phi+1,\ell} - (\phi_{\max} + \phi)m_{\phi,\ell}]}_{\text{resolving phenotype modulation}} \\
 & + \underbrace{R_{\phi,\ell}(t)}_{\text{recruitment}} - \underbrace{(\beta + \gamma)m_{\phi,\ell}}_{\text{apoptosis and egress}},
 \end{aligned} \tag{1}$$

and closure conditions:

$$m_{\phi,-1} \equiv m_{\phi,\ell_{\max}+1} \equiv m_{-\phi_{\max}-1,\ell} \equiv m_{\phi_{\max}+1,\ell} \equiv 0, \tag{2}$$

for every $\phi = 0, \pm 1, \dots, \pm\phi_{\max}$ and $\ell = 0, 1, \dots, \ell_{\max}$.

The first term on the right hand side of Eq. (1) accounts for lipid uptake. Following Chambers et al. (2023), we model lipid uptake with a mass-action treatment of the following reactions:



for every (ϕ, ℓ) and $i \in \{LDL, r, ap, n\}$. Reactions (3) assume that the rate of lipid uptake decreases linearly with lipid content in a manner commensurate with available capacity. For notational brevity in Eq. (1), we introduce vectors for the uptake rates, $\mathbf{k}_L := (k_{LDL}, k_r, k_{ap}, k_n)$, and the extracellular lipids, $\mathbf{L} := (L_{LDL}, L_r, L_{ap}, L_n)$, so that $\mathbf{k}_L \cdot \mathbf{L} = k_{LDL}L_{LDL} + k_rL_r + k_{ap}L_{ap} + k_nL_n$.

The second term of the RHS of Eq. (1) accounts for lipid efflux to HDL. Again, following Chambers et al. (2023), we treat efflux with mass-action kinetics according to the reactions:

$$m_{\phi, \ell}(t) + H(t)/\Delta a \xrightarrow{k_H \ell} m_{\phi, \ell-1}(t), \tag{4}$$

for every (ϕ, ℓ) . The reactions (4) assume that the efflux rate increases linearly with lipid content.

The third and fourth terms of the RHS of Eq. (1) account for MDM phenotype modulation by inflammatory and resolving mediators (Bäck et al. 2019), S_+ and S_- respectively. We model phenotype modulation via the reactions:

$$m_{\phi, \ell}(t) + S_{\pm}(t)/\Delta s \xrightarrow{k_S} \begin{cases} m_{\phi \pm 1, \ell}(t) & \text{w/ probability } p_{\phi}^{\pm} := \chi(\phi_{\max} \mp \phi) \\ m_{\phi, \ell}(t) & \text{w/ probability } 1 - p_{\phi}^{\pm}, \end{cases} \tag{5}$$

for every (ϕ, ℓ) . Here k_S is the rate of mediator binding to MDM surface receptors and Δs is the mediator mass bound per interaction. We assume each mediator binding interaction stimulates a move to a new phenotype class with probability: $p_{\phi}^{\pm} = \chi(\phi_{\max} \mp \phi)$. The parameter $0 \leq \chi \leq (2\phi_{\max})^{-1}$ which modulates this probability can be interpreted as the phenotypic plasticity of the MDMs. We assume that p_{ϕ}^{\pm} decreases linearly to zero as $\phi \rightarrow \pm\phi_{\max}$, so that it becomes increasingly difficult for MDMs to become more polarised the more polarised they are. Biologically, this property reflects the saturation of intracellular signalling pathways when macrophages are continually exposed to inflammatory or resolving mediators.

The final terms on the RHS of Eq. (1) account for MDM recruitment, apoptosis and egress. We assume that newly recruited MDMs enter the lesion from the bloodstream carrying only endogenous lipid and with an uncommitted phenotype:

$$R_{\phi, \ell}(t) := \begin{cases} \sigma_M \left(\frac{S_+}{S_+ + S_+^{50} + \rho S_-} \right) & \text{if } (\phi, \ell) = (0, 0); \\ 0 & \text{if } (\phi, \ell) \neq (0, 0). \end{cases} \tag{6}$$

The recruitment rate is a first-order Hill function of the inflammatory mediator density, S_+ , which saturates at the maximum value σ_M . Resolving mediators, S_- , inhibit recruitment by linearly increasing the threshold for half-maximal recruitment from the basal value S_+^{50} ; the parameter ρ governs the sensitivity of the recruitment rate to S_- . We assume for simplicity that the rates of MDM apoptosis, β , and egress, γ , are constant.

Extracellular lipids. We assume that the densities of free and retained LDL evolve according to the ODEs:

$$\begin{aligned} \frac{dL_{LDL}}{dt} = & \underbrace{\pi_L^{(0)}(L^{(0)} - L_{LDL})}_{\text{luminal flux}} - \underbrace{\pi_L^{(1)}(L_{LDL} - L^{(1)})}_{\text{tunica media flux}} \\ & - \underbrace{k_b L_{LDL}(K_r - L_r)}_{\text{retention via ECM binding}} + \underbrace{k_{-b} L_r}_{\text{unbinding}} \\ & - \underbrace{k_{LDL} \Delta a L_{LDL} \sum_{\phi, \ell} (\ell_{\max} - \ell) m_{\phi, \ell}}_{\text{uptake by MDMs}}, \end{aligned} \tag{7}$$

$$\begin{aligned} \frac{dL_r}{dt} = & +k_b L_{LDL}(K_r - L_r) - k_{-b} L_r \\ & - k_r \Delta a L_r \sum_{\phi, \ell} (\ell_{\max} - \ell) m_{\phi, \ell}. \end{aligned} \tag{8}$$

The first two terms on the RHS of Eq. (7) account for the flux of free LDL between the lesion and the lumen/tunica media. The parameters $\pi_L^{(0)}$ and $\pi_L^{(1)}$ denote the LDL exchange rate at the endothelium and internal elastic lamina, respectively. The densities of free LDL in the lumen, $L^{(0)}$, and tunica media, $L^{(1)}$, are assumed to be non-negative constants. We assume that free LDL binds to ECM proteoglycans with rate constant k_b in a capacity-limited manner, and unbinds at rate k_{-b} ; the maximum capacity for LDL retention is K_r . The final terms on the RHS of Eqs. (7) and (8) account for MDM uptake of free and bound LDL via reactions (3).

We propose that the densities of apoptotic and necrotic lipid satisfy:

$$\frac{dL_{ap}}{dt} = \underbrace{\beta \sum_{\phi, \ell} (a_0 + \ell \Delta a) m_{\phi, \ell}}_{\text{apoptosis}} - \nu L_{ap} - k_{ap} \Delta a L_{ap} \sum_{\phi, \ell} (\ell_{\max} - \ell) m_{\phi, \ell}, \tag{9}$$

$$\frac{dL_n}{dt} = \beta \sum_{\phi, \ell} (a_0 + \ell \Delta a) m_{\phi, \ell} + \underbrace{\nu L_{ap}}_{\text{necrosis}} - \underbrace{k_n \Delta a L_n \sum_{\phi, \ell} (\ell_{\max} - \ell) m_{\phi, \ell}}_{\text{uptake by MDMs}}. \tag{10}$$

The first term of the RHS of Eq. (9) accounts for lipid deposition into the extracellular space due to MDM apoptosis. We assume that apoptotic cells undergo secondary necrosis at rate ν , which provide linear sink and source terms in Eqs. (9) and (10), respectively. The final terms on the RHS of Eqs. (9) and (10) describe apoptotic and necrotic lipid uptake by MDMs.

HDL lipid capacity. We assume that the lipid capacity of the HDL particles in the lesion evolves according to:

$$\frac{dH}{dt} = \underbrace{\pi_H^{(0)}(H^{(0)} - H)}_{\text{luminal flux}} - \underbrace{\pi_H^{(1)}(H - H^{(1)})}_{\text{tunica media flux}} - \underbrace{k_H \Delta a H \sum_{\phi, \ell} \ell m_{\phi, \ell}}_{\text{lipid efflux by MDMs}}. \tag{11}$$

The first two terms on the RHS of Eq. (11) describe the flux of HDL lipid capacity (via HDL particle diffusion) between the lesion and the lumen/tunica media. For simplicity, we assume that the diffusivity of HDL particles is independent of their lipid capacity, so that $\pi_H^{(0)}$ and $\pi_H^{(1)}$ represent the common permeability of HDL particles and HDL lipid capacity at the endothelium and internal elastic lamina respectively. The final term accounts for MDM lipid efflux to HDL particles.

Inflammatory and resolving mediators. We propose that the densities of inflammatory and resolving mediators satisfy the following ODEs:

$$\begin{aligned} \frac{dS_+}{dt} = & \underbrace{\alpha L_r}_{\text{resident signals}} + \underbrace{\mu \left[(k_{LDL} L_{LDL} + k_r L_r) \Delta a \sum_{\phi, \ell} (\ell_{\max} - \ell) m_{\phi, \ell} + \nu L_{ap} \right]}_{\text{LDL-stimulated emission}} \underbrace{\phantom{\mu \left[(k_{LDL} L_{LDL} + k_r L_r) \Delta a \sum_{\phi, \ell} (\ell_{\max} - \ell) m_{\phi, \ell} + \nu L_{ap} \right]}}_{\text{DAMPs}} \\ & + \underbrace{k_c \sum_{\phi, \ell} \left(1 + \frac{\phi}{\phi_{\max}} \right) m_{\phi, \ell}}_{\text{MDM constitutive production}} - \underbrace{\left[k_S \Delta s \sum_{\phi, \ell} m_{\phi, \ell} + \delta_S \right] S_+}_{\text{MDM binding and decay}}, \end{aligned} \tag{12}$$

$$\begin{aligned} \frac{dS_-}{dt} = & \underbrace{\mu \left[k_{ap} \Delta a L_{ap} \sum_{\phi, \ell} (\ell_{\max} - \ell) m_{\phi, \ell} + k_H \Delta a H \sum_{\phi, \ell} \ell m_{\phi, \ell} \right]}_{\text{efferocytosis-stimulated emission}} \underbrace{\phantom{\mu \left[k_{ap} \Delta a L_{ap} \sum_{\phi, \ell} (\ell_{\max} - \ell) m_{\phi, \ell} + k_H \Delta a H \sum_{\phi, \ell} \ell m_{\phi, \ell} \right]}}_{\text{HDL-stimulated emission}} \\ & + \underbrace{k_c \sum_{\phi, \ell} \left(1 - \frac{\phi}{\phi_{\max}} \right) m_{\phi, \ell}}_{} - \underbrace{\left[k_S \Delta s \sum_{\phi, \ell} m_{\phi, \ell} + \delta_S \right] S_-}_{}. \end{aligned} \tag{13}$$

The first term on the RHS of Eq. (12) models the release of inflammatory signals by resident cells (e.g. smooth muscle cells, tissue-resident macrophages) (Williams et al. 2019, 2020). The signal cascades which first stimulate MDM recruitment are, as yet, unknown, but are thought to be the result of excessive LDL retention (Williams and Tabas 2005). Hence, we assume for simplicity that the resident cells produce inflammatory mediators at rate proportional to the retained LDL lipid density.

Equations (12) and (13) also account for mediator production due to lipid activity. This includes MDM production of inflammatory mediators due to LDL uptake (both native and modified forms of LDL induce inflammatory responses in macrophages (Allen et al. 2022; Chen and Khismatullin 2015)), and MDM production of resolving mediators upon apoptotic lipid uptake (Dalli and Serhan 2012) and interaction with HDL (Serhan and Levy 2018). We also include production of inflammatory DAMPs that are released by apoptotic bodies upon secondary necrosis (Sachet et al. 2017). We

assume for simplicity that the magnitude of mediator production is proportional to the amount of lipid involved in each of the above interactions; the parameter μ represents the mediator mass produced per unit lipid.

The remaining source terms in Eqs. (12) and (13) account for constitutive mediator production by MDMs. Indeed, macrophages are potent cytokine emitters (even in the absence of stimulants (Chen and Khisimatullin 2015)) and exhibit a phenotype-dependent secretion profile (Kadomoto et al. 2021). To account for these effects, we assume that MDMs constitutively produce mediators at the constant rate $2k_c$ per cell, but that the ratio of inflammatory to resolving mediator production is skewed linearly according to phenotype. M1-polarised cells with $\phi = \phi_{\max}$ secrete only inflammatory mediators while M2-polarised cells with $\phi = -\phi_{\max}$ emit only resolving mediators.

We further assume that mediators bind to MDM surface receptors, according to reaction (5), and undergo natural decay at rate δ_S . We use a common decay rate for both inflammatory and resolving mediators since experimentally reported half-lives for inflammatory and resolving cytokines are comparable (Liu et al. 2021). Similarly, we use a common binding rate in the absence of evidence for MDM preferential binding.

Initial conditions We close Eqs. (1), (7)–(13) by supposing that at $t = 0$:

$$\begin{aligned}
 m_{\phi,\ell} &= 0 \quad \text{for every } (\phi, \ell), \\
 L_{LDL} &= \frac{\pi_L^{(0)} L^{(0)} + \pi_L^{(1)} L^{(1)}}{\pi_L^{(0)} + \pi_L^{(1)}}, \quad L_r = \frac{k_b L_{LDL} K_r}{k_b L_{LDL} + k_{-b}}, \quad L_{ap} = L_n = 0, \\
 H &= \frac{\pi_H^{(0)} H^{(0)} + \pi_H^{(1)} H^{(1)}}{\pi_H^{(0)} + \pi_H^{(1)}}, \quad S_+ = \frac{\alpha L_r}{\delta_S}, \quad S_- = 0.
 \end{aligned} \tag{14}$$

The conditions (42) describe the atherosclerotic lesion immediately prior to MDM recruitment. These expressions are derived by solving Eqs. (1), (7)–(13) at steady state with $m_{\phi,\ell} = 0$ for every (ϕ, ℓ) . We find that free LDL lipid and HDL lipid capacity are balanced by their fluxes at the endothelium and internal elastic lamina. Retained LDL levels reflect a balance of binding/unbinding kinetics and directly scale inflammatory mediator levels. The remaining variables are initially zero.

2.3 A Closed Subsystem

We can derive a closed subsystem from Eqs. (1), (7)–(13) by defining the population variables:

$$M(t) := \sum_{\phi,\ell} m_{\phi,\ell}(t), \tag{15}$$

$$\hat{\Phi}_M(t) := \frac{1}{M(t)} \sum_{\phi,\ell} \left(\frac{\phi}{\phi_{\max}} \right) m_{\phi,\ell}(t), \tag{16}$$

$$\hat{L}_M(t) := \frac{1}{M(t)} \sum_{\phi,\ell} \left(\frac{\ell}{\ell_{\max}} \right) m_{\phi,\ell}(t). \tag{17}$$

Here $M(t) \geq 0$ represents the total MDM density. The quantity $-1 \leq \hat{\Phi}_M(t) \leq 1$ is the mean MDM phenotype, normalised such that $\hat{\Phi}_M = 1$ corresponds to M1-polarisation and $\hat{\Phi}_M = -1$ to M2-polarisation. Finally, $0 \leq \hat{L}_M(t) \leq 1$ is the mean MDM lipid content, normalised by the maximal capacity.

By differentiating definitions (15)–(17) with respect to time and substituting from Eq. (1), we obtain ODEs for M , $\hat{\Phi}_M$ and \hat{L}_M :

$$\frac{dM}{dt} = \left(\frac{\sigma_M S_+}{S_+ + S_+^{c50} + \rho S_-} \right) - (\beta + \gamma)M, \tag{18}$$

$$\frac{d\hat{\Phi}_M}{dt} = k_s \chi [S_+(1 - \hat{\Phi}_M) - S_-(1 + \hat{\Phi}_M)] - \left(\frac{\sigma_M S_+}{S_+ + S_+^{c50} + \rho S_-} \right) \frac{\hat{\Phi}_M}{M}, \tag{19}$$

$$\frac{d\hat{L}_M}{dt} = k_L \cdot L (1 - \hat{L}_M) - k_H H \hat{L}_M - \left(\frac{\sigma_M S_+}{S_+ + S_+^{c50} + \rho S_-} \right) \frac{\hat{L}_M}{M}. \tag{20}$$

Sink terms arise in Eqs. (19) and (20) because recruited MDMs enter the lesion with $\phi = \ell = 0$, reducing the mean (absolute) phenotype and lipid content. We can also rewrite Eqs. (7)–(13) as follows:

$$\begin{aligned} \frac{dL_{LDL}}{dt} &= \pi_L^{(0)}(L^{(0)} - L_{LDL}) - \pi_L^{(1)}(L_{LDL} - L^{(1)}) \\ &\quad - k_b L_{LDL}(K_r - L_r) + k_{-b} L_r - k_{LDL} \kappa L_{LDL} M(1 - \hat{L}_M), \end{aligned} \tag{21}$$

$$\frac{dL_r}{dt} = k_b L_{LDL}(K_r - L_r) - k_{-b} L_r - k_r \kappa L_r M(1 - \hat{L}_M), \tag{22}$$

$$\frac{dL_{ap}}{dt} = \beta M(1 + \kappa \hat{L}_M) - \nu L_{ap} - k_{ap} \kappa L_{ap} M(1 - \hat{L}_M), \tag{23}$$

$$\frac{dL_n}{dt} = \nu L_{ap} - k_n \kappa L_n M(1 - \hat{L}_M), \tag{24}$$

$$\frac{dH}{dt} = \pi_H^{(0)}(H^{(0)} - H) - \pi_L^{(1)}(H - H^{(1)}) - k_H \kappa H M \hat{L}_M, \tag{25}$$

$$\begin{aligned} \frac{dS_+}{dt} &= \alpha L_r + \mu \left[(k_{LDL} L_{LDL} + k_r L_r) \kappa M(1 - \hat{L}_M) + \nu L_{ap} \right] \\ &\quad + k_c M(1 + \hat{\Phi}_M) - (k_S \Delta s M + \delta_S) S_+, \end{aligned} \tag{26}$$

$$\begin{aligned} \frac{dS_-}{dt} &= \mu \left[k_{ap} \kappa L_{ap} M(1 - \hat{L}_M) + k_H \kappa H M \hat{L}_M \right] \\ &\quad + k_c M(1 - \hat{\Phi}_M) - (k_S \Delta s M + \delta_S) S_-. \end{aligned} \tag{27}$$

Equations (18)–(27) with the initial conditions (14) comprise a closed subsystem that can be solved independently of Eq. (1).

2.4 Parameter Values

The parameters that appear in Eqs. (1), (18)–(27) are summarised in Table 1.

Table 1 Model parameters

Parameter	Interpretation	Estimate	Source
$L^{(0)}$	Lumen LDL lipid density	0–440 mg/dL	Lee et al. (2012); Orlova et al. (1999)
$H^{(0)}$	Lumen HDL lipid capacity	0–230 mg/dL	Madsen et al. (2017)
$\pi_L^{(0)}$	Endothelial LDL exchange rate	1.5 month ⁻¹	Nielsen (1996); Holzapfel et al. (2005)
$\pi_H^{(0)}$	Endothelial HDL exchange rate	3.0 month ⁻¹	Stender and Zilversmit (1981), $\approx 2\pi_L^{(0)}$
$L^{(1)}$	Tunica media LDL lipid density	0 mg/dL	Smith and Staples (1982)
$H^{(1)}$	Tunica media HDL lipid capacity	0 mg/dL	Smith and Staples (1982), est
$\pi_L^{(1)}$	Internal elastic lamina LDL exchange rate	4.5 month ⁻¹	Penn et al. (1994), $\approx 3\pi_L^{(0)}$
$\pi_H^{(1)}$	Internal elastic lamina HDL exchange rate	9.0 month ⁻¹	Penn et al. (1994), $\approx 3\pi_H^{(0)}$
K_r	LDL retention capacity	15–7500 mg/dL	Wight (2018); Guyton and Klemp (1989); Liu et al. (2023)
k_b	LDL retention rate	0.008 dL/mg month ⁻¹	Bancells et al. (2009); Smith and Staples (1982)
k_{-b}	LDL unbinding rate	1.8 month ⁻¹	Bancells et al. (2009); Smith and Staples (1982)
σ_M	Maximum MDM entry rate	19000 mm ⁻³ month ⁻¹	Williams et al. (2009); Nelson (2014); Lee et al. (2019)
β	MDM apoptosis rate	1.0 month ⁻¹	Yona et al. (2013); Williams et al. (2020)
γ	MDM egress rate	0.2 month ⁻¹	Williams et al. (2018); Lee et al. (2019), est

Table 1 continued

Parameter	Interpretation	Estimate	Source
ν	Secondary necrosis rate	37 month^{-1}	Saraste and Pulkki (2000)
a_0	MDM endogenous lipid	55pg	Sokol et al. (1991); Cooper and Adams (2022)
κ	MDM lipid capacity	1600pg	Ford et al. (2019), $\approx 29a_0$
k_{LDL}	LDL lipid uptake rate	$0.00034 \text{ dL/mg month}^{-1}$	Sanda et al. (2021)
k_r	rLDL lipid uptake rate	$0.023 \text{ dL/mg month}^{-1}$	Sanda et al. (2021)
k_{ap}	Apoptotic lipid uptake rate	$0.060 \text{ dL/mg month}^{-1}$	Taruc et al. (2018); Schrijvers et al. (2005)
k_n	Necrotic lipid uptake rate	$0.015 \text{ dL/mg month}^{-1}$	Brouckaert et al. (2004), $\approx k_{ap}/4$
k_H	Lipid efflux rate	$0.34 \text{ dL/mg month}^{-1}$	Krihtharides et al. (1998); Woudberg et al. (2018)
S_c^{50}	Mediator density for half-maximum MDM recruitment	5 ng/mL	O'Carroll et al. (2015); Pugin et al. (1993)
ρ	Sensitivity of MDM recruitment to resolving mediators	0.40	Sha et al. (2015)
δ_S	Mediator natural decay rate	1600 month^{-1}	Liu et al. (2021)
Δ_S	Mediator mass	17 kDa	Atzeni and Sarzi-Puttini (2013)
k_S	Mediator binding rate to MDM surface receptors	$8800 \text{ mL/ng month}^{-1}$	Watanabe et al. (1988); Niitsu et al. (1988)
k_C	Constitutive mediator production rate by MDMs	$1.5 \text{ pg month}^{-1}$	Schutte et al. (2009)
μ	Mediator production per unit lipid stimulus	0.042	Schutte et al. (2009)
α	Resident inflammatory mediator production per rLDL lipid	$3.5 \times 10^{-3} \text{ month}^{-1}$	Williams et al. (2020)
χ	MDM phenotypic plasticity	6.0×10^{-6}	Tarique et al. (2015)
Δa	MDM uptake/efflux increment of lipid	16 pg	Kontush et al. (2007); Taefehshokr et al. (2021), $\in (75\text{kDa}, a_0)$
ℓ_{\max}	Maximum MDM lipid capacity per uptake/efflux increment	100	$= \kappa/\Delta a$
ϕ_{\max}	Half the maximum number of MDM phenotype classes	50	$< (2\chi)^{-1}$

The blood densities of LDL lipid, $L^{(0)}$, and HDL lipid capacity, $H^{(0)}$, are key parameters in our model. Since these quantities are sensitive to modifiable lifestyle factors such as diet and exercise (Schoeneck and Iggman 2021), we explore a range of plausible values in our analysis. The range for $L^{(0)}$ is based on the human serum LDL cholesterol distribution reported in Lee et al. (2012), in which 99.8% of the subjects had LDL cholesterol below 280mg/dL. We multiply this figure by 78/50 to account for LDL phospholipid to obtain an upper estimate of 480mg/dL (Orlova et al. 1999). We take $H^{(0)} = 230\text{mg}$ as a conservative upper bound, which exceeds the highest recorded HDL cholesterol concentrations (193 mg/dL) in a sample of 116508 individuals from the general population (Madsen et al. 2017).

We consider a range of values for the LDL retention capacity, K_r , since it varies between artery wall sections (Lewis et al. 2023). As LDL retention is driven by LDL-proteoglycan binding, we estimate K_r by considering the artery wall proteoglycan density. Artery wall extracellular matrix prior to atherosclerosis-induced collagen degradation consists of 4% proteoglycan and 40% collagen (Wight 2018). Using 0.01–3 mg/mL as an estimate for the collagen density (0.75 mg/mL is used to replicate the tunica intima in culture models (Liu et al. 2023)), we obtain a proteoglycan density of 0.001–0.3 mg/mL. Assuming each proteoglycan molecule (est. mass 800kDa (Yoneda et al. 2002)) can support a single aggregate of LDL (typical diameter 75nm, corresponding to 0.0002 pg lipid for spherical droplets (Guyton and Klemp 1989)), we estimate $K_r \approx 15 - 4500 \text{ mg/dL}$.

The values of the remaining parameters are fixed. See Appendix A for further details on these choices of parameter values.

2.5 Non-dimensionalisation

We recast the model in terms of the following dimensionless variables:

$$\begin{aligned}
 \tilde{t} &:= \beta t, & \tilde{m}_{\phi,\ell}(\tilde{t}) &:= \frac{\beta}{\sigma_M} m_{\phi,\ell}(t), & \tilde{M}(\tilde{t}) &:= \frac{\beta}{\sigma_M} M(t), \\
 \tilde{\mathbf{L}}(\tilde{t}) &:= \frac{\beta}{a_0\sigma_M} \mathbf{L}(t), & \tilde{H}(\tilde{t}) &:= \frac{\beta}{a_0\sigma_M} H(t), & \tilde{S}_{\pm}(\tilde{t}) &:= \frac{1}{S_+^{c50}} S_{\pm}(t).
 \end{aligned} \tag{28}$$

This scaling measures time in units of mean MDM lifespan, $\beta^{-1} \approx 1\text{month}$, and MDM densities relative to the maximum influx per MDM lifespan, $\sigma_M\beta^{-1} \approx 17000 \text{ mm}^{-3}$. We express the extracellular lipid densities and HDL lipid capacity relative to the maximum influx of MDM endogenous lipid per MDM lifespan, $a_0\sigma_M\beta^{-1} \approx 45 \text{ mg/dL}$. Mediator densities are measured relative to the density for half-maximal MDM recruitment, $S_+^{c50} \approx 5 \text{ ng/mL}$. We also introduce a number of dimensionless parameters in Table 2.

Applying the non-dimensionalisation (28) and definitions of Table 2, and dropping the tildes for notational convenience, we obtain the following dimensionless ODEs

Table 2 Dimensionless parameters in the rescaled Eqs. (29)–(41)

Parameter	Definition	Interpretation	Estimate
\tilde{L}^*	$\frac{\beta}{a_0\sigma_M} L^{(0)}$	Lumen LDL lipid density	0–10
\tilde{H}^*	$\frac{\beta}{a_0\sigma_M} H^{(0)}$	Lumen HDL lipid capacity	0–5
\tilde{K}_r	$\frac{\beta}{a_0\sigma_M} K_r$	LDL retention capacity	0.3–100
$\tilde{\pi}_L^{(0)}$	$\frac{1}{\beta} \pi_L^{(0)}$	Endothelial LDL exchange rate	1.5
$\tilde{\pi}_H^{(0)}$	$\frac{1}{\beta} \pi_H^{(0)}$	Endothelial HDL exchange rate	3.0
$\tilde{\pi}_L^{(1)}$	$\frac{1}{\beta} \pi_L^{(1)}$	Internal elastic lamina LDL exchange rate	4.5
$\tilde{\pi}_H^{(1)}$	$\frac{1}{\beta} \pi_H^{(1)}$	Internal elastic lamina HDL exchange rate	9.0
\tilde{k}_b	$\frac{a_0\sigma_M}{\beta^2} k_b$	LDL retention rate	2.7
\tilde{k}_{-b}	$\frac{1}{\beta} k_{-b}$	LDL unbinding rate	1.8
$\tilde{\gamma}$	$\frac{1}{\beta} \gamma$	MDM egress rate	0.2
$\tilde{\nu}$	$\frac{1}{\beta} \nu$	Secondary necrosis rate	37
$\tilde{\kappa}$	$\frac{1}{a_0} \kappa$	MDM lipid capacity per unit endogenous lipid	29
\tilde{k}_{LDL}	$\frac{a_0\sigma_M}{\beta^2} k_{LDL}$	LDL uptake rate	0.016
\tilde{k}_r	$\frac{a_0\sigma_M}{\beta^2} k_r$	rLDL uptake rate	1.1
\tilde{k}_{ap}	$\frac{a_0\sigma_M}{\beta^2} k_{ap}$	Apoptotic lipid uptake rate	5.5
\tilde{k}_n	$\frac{a_0\sigma_M}{\beta^2} k_n$	Necrotic lipid uptake rate	1.4
\tilde{k}_H	$\frac{a_0\sigma_M}{\beta^2} k_H$	Lipid efflux rate	16
$\tilde{\rho}$	ρ	MDM influx sensitivity to resolving mediators	0.4
\tilde{k}_S	$\frac{\sigma_M \Delta S}{\beta^2} k_S$	Mediator binding rate to MDM receptors	47
$\tilde{\delta}_S$	$\frac{1}{\beta} \delta_S$	Mediator natural decay rate	1600
\tilde{k}_c	$\frac{\sigma_M}{S c_+^{50} \beta^2} k_c$	Constitutive MDM mediator production rate	5100
$\tilde{\mu}$	$\frac{a_0\sigma_M}{S c_+^{50} \beta} \mu$	Lipid-stimulated mediator production	9200
$\tilde{\alpha}$	$\frac{a_0\sigma_M}{S c_+^{50} \beta^2} \alpha$	Resident mediator production per rLDL lipid	850
$\tilde{\chi}$	$\frac{k_S S c_+^{50}}{\sigma_M} \chi$	MDM phenotypic plasticity	0.28
ϕ_{max}	ϕ_{max}	MDM phenotype resolution	50
ℓ_{max}	ℓ_{max}	MDM maximum lipid capacity	100

for the MDM population:

$$\begin{aligned}
 \frac{d}{dt} m_{\phi, \ell} = & k_L \cdot L [(\ell_{max} - \ell + 1)m_{\phi, \ell-1} - (\ell_{max} - \ell)m_{\phi, \ell}] \\
 & + k_H H [(\ell + 1)m_{\phi, \ell+1} - \ell m_{\phi, \ell}] \\
 & + \chi S_+ [(\phi_{max} - \phi + 1)m_{\phi-1, \ell} - (\phi_{max} - \phi)m_{\phi, \ell}] \\
 & + \chi S_- [(\phi_{max} + \phi + 1)m_{\phi+1, \ell} - (\phi_{max} + \phi)m_{\phi, \ell}] \\
 & + R_{\phi, \ell} - (1 + \gamma)m_{\phi, \ell},
 \end{aligned} \tag{29}$$

where:

$$R_{\phi, \ell} := \begin{cases} \frac{S_+}{S_+ + 1 + \rho S_-} & \text{if } (\phi, \ell) = (0, 0); \\ 0 & \text{if } (\phi, \ell) \neq (0, 0), \end{cases} \tag{30}$$

$$m_{\phi, -1} \equiv m_{\phi, \ell_{\max} + 1} \equiv m_{-\phi_{\max} - 1, \ell} \equiv m_{\phi_{\max} + 1, \ell} \equiv 0, \tag{31}$$

for every $\phi = 0, \pm 1, \dots, \pm \phi_{\max}$ and $\ell = 0, 1, \dots, \ell_{\max}$. The remaining variables solve the closed subsystem:

$$\frac{dM}{dt} = \frac{S_+}{S_+ + 1 + \rho S_-} - (1 + \gamma)M, \tag{32}$$

$$\frac{d\hat{\Phi}_M}{dt} = \chi[S_+(1 - \hat{\Phi}_M) - S_-(1 + \hat{\Phi}_M)] - \left(\frac{S_+}{S_+ + 1 + \rho S_-}\right) \frac{\hat{\Phi}_M}{M}, \tag{33}$$

$$\frac{d\hat{L}_M}{dt} = k_L \cdot L(1 - \hat{L}_M) - k_H H \hat{L}_M - \left(\frac{S_+}{S_+ + 1 + \rho S_-}\right) \frac{\hat{L}_M}{M}, \tag{34}$$

$$\begin{aligned} \frac{dL_{LDL}}{dt} &= \pi_L^{(0)}(L^* - L_{LDL}) - \pi_L^{(1)}L_{LDL} \\ &\quad - k_b L_{LDL}(K_r - L_r) + k_{-b}L_r - k_{LDL\kappa}L_{LDL}M(1 - \hat{L}_M), \end{aligned} \tag{35}$$

$$\frac{dL_r}{dt} = k_b L_{LDL}(K_r - L_r) - k_{-b}L_r - k_r\kappa L_r M(1 - \hat{L}_M), \tag{36}$$

$$\frac{dL_{ap}}{dt} = M(1 + \kappa \hat{L}_M) - \nu L_{ap} - k_{ap\kappa}L_{ap}M(1 - \hat{L}_M), \tag{37}$$

$$\frac{dL_n}{dt} = \nu L_{ap} - k_n\kappa L_n M(1 - \hat{L}_M), \tag{38}$$

$$\frac{dH}{dt} = \pi_H^{(0)}(H^* - H) - \pi_L^{(1)}H - k_H\kappa H M \hat{L}_M, \tag{39}$$

$$\begin{aligned} \frac{dS_+}{dt} &= \alpha L_r + \mu \left[(k_{LDL}L_{LDL} + k_r L_r)\kappa M(1 - \hat{L}_M) + \nu L_{ap} \right] \\ &\quad + k_c M(1 + \hat{\Phi}_M) - (k_S M + \delta_S)S_+, \end{aligned} \tag{40}$$

$$\begin{aligned} \frac{dS_-}{dt} &= \mu \left[k_{ap\kappa}L_{ap}M(1 - \hat{L}_M) + k_H\kappa H M \hat{L}_M \right] \\ &\quad + k_c M(1 - \hat{\Phi}_M) - (k_S M + \delta_S)S_-. \end{aligned} \tag{41}$$

Finally, we assume that at $t = 0$:

$$\begin{aligned} m_{\phi, \ell} &= 0 \text{ for every } (\phi, \ell), \\ L_{LDL} &= \frac{\pi_L^* L^*}{\pi_L^{(0)} + \pi_L^{(1)}}, & L_r &= \frac{k_b L_{LDL} K_r}{k_b L_{LDL} + k_{-b}}, & L_{ap} &= L_n = 0, \\ H &= \frac{\pi_H^{(0)} H^*}{\pi_H^{(0)} + \pi_H^{(1)}}, & S_+ &= \frac{\alpha L_r}{\delta_S}, & S_- &= 0. \end{aligned} \tag{42}$$

2.6 Numerical Solutions and Timescales

The dimensionless parameters in Table 2 span several orders of magnitude. In particular, the mediator parameters α , δ_S , k_S and μ are considerably larger than the other constants. Numerical solutions of Eqs. (29)–(41) consequently require small timesteps to maintain stability. We address this issue in our numerical solutions, computed with Wolfram Mathematica, by using the routine *NDSolve* with the “StiffnessSwitching” option.

Another way to reduce numerical stiffness is to approximate the mediator dynamics via separation of timescales. With $\delta_S^{-1} \ll 1$ and assuming that α , k_S , $\mu = \mathcal{O}(\delta_S)$, it is straightforward to show that S_{\pm} satisfy the following uniformly-valid quasi-steady state approximations:

$$S_+ \sim \hat{\alpha}L_r + \hat{\mu}[(k_{LDL}L_{LDL} + k_rL_r)\kappa M(1 - \hat{L}_M) + \nu L_{ap}] + \hat{k}_cM(1 + \hat{\Phi}_M), \tag{43}$$

$$S_- \sim \hat{\mu}\kappa M[k_{ap}L_{ap}(1 - \hat{L}_M) + k_H H \hat{L}_M] + \hat{k}_cM(1 - \hat{\Phi}_M), \text{ as } \delta_S^{-1} \rightarrow 0, \tag{44}$$

where $\hat{\alpha} := \alpha/\delta_S$, $\hat{\mu} := \mu/\delta_S$ and $\hat{k}_c := k_c/\delta_S$. Although approximations (43)–(44) are not used for the simulations presented in Sect. 3, they reveal that, at leading order, the mediator densities are proportional to their net rates of production.

3 Results

We present the results in two sections. In Sect. 3.1 we analyse the subsystem (32)–(41) to generate insight into lesion composition. In Sect. 3.2 we focus on the MDM phenotype-lipid distribution, $m_{\phi,\ell}$.

3.1 Lesion Composition

We begin our analysis of lesion composition by computing time-dependent solutions of the subsystem (32)–(41); the results are presented in Sect. 3.1.1. In Sect. 3.1.2 we then analyse the impact of the key parameters: L^* , H^* and K_r on the steady state values.

3.1.1 Time Evolution

Two typical numerical solutions of the subsystem (32)–(41) are shown in Fig. 3. The left and right solutions respectively correspond to healthy ($L^* = 3$, $H^* = 2.5$) and unhealthy ($L^* = 4.5$, $H^* = 1$) blood levels of LDL lipid and HDL capacity. We set $K_r = 10$ for both cases. The quantity $L(t)$ in plots (d) and (i) is the total extracellular lipid density:

$$L(t) := L_{LDL}(t) + L_r(t) + L_{ap}(t) + L_n(t), \tag{45}$$

whereas plots (e) and (j) show the components of the total lesion lipid content:

$$L_{\text{tot}}(t) := L_{\text{LDL}}(t) + L_{\text{r}}(t) + [1 + \kappa \hat{L}_M(t)]M(t) + L_{\text{ap}}(t) + L_{\text{n}}(t), \tag{46}$$

which includes MDM lipid. The model dynamics can be broadly divided into three phases that we detail below.

The first weeks after initial MDM influx ($0 < t < 0.2$) are characterised by a decline in lesion LDL and rLDL content (Fig. 3e, j). Both reductions are driven by MDM uptake of rLDL, which also promotes binding of free LDL by restoring the LDL retention capacity. The rise in \hat{L}_M is accompanied by increases in $\hat{\Phi}_M$ and S_+ since rLDL uptake stimulates production of inflammatory mediators that drive inflammatory phenotype modulation (see Fig. 3b, c, g, h).

For $0.2 < t < 2$, the growth of \hat{L}_M and S_+ slows and $\hat{\Phi}_M$ decreases (see Fig. 3b, c, g, h). These behaviours arise because the MDM population has ingested enough lipid for the lipid efflux rate to become comparable to that of uptake. For both simulations, the efflux rate exceeds the uptake rate at $t \approx 0.5$, where \hat{L}_M attains a local maximum. The corresponding increase in resolving mediators, S_- , relative to inflammatory mediators, S_+ , promotes resolving phenotype modulation.

For $2 < t < \infty$, the model tends to a non-zero steady state in a manner sensitive to parameter values. For healthier balances of blood LDL lipid and HDL capacity (L^*, H^*): mean MDM lipid content declines to a small non-zero value and mean MDM phenotype remains negative (i.e. resolving) (Fig. 3b), resolving mediators outbalance inflammatory mediators (Fig. 3c), extracellular lipid levels are low while HDL capacity remains substantial (Fig. 3d), and lesion lipid content decreases to densities below those prior to MDM influx (Fig. 3e). By contrast, when L^* is sufficiently high relative to H^* (quantified in Sect. 3.1.2): MDM densities are greater (Fig. 3f), mean MDM lipid content increases to a large value and mean MDM phenotype is positive (i.e. inflammatory) (Fig. 3g), inflammatory mediators outbalance resolving mediators (Fig. 3h), HDL capacity is largely exhausted while extracellular lipid levels remain substantial (Fig. 3i), and lesion lipid densities increase to values higher than those prior to initial MDM influx (Fig. 3j).

In Fig. 4 we show how the LDL retention capacity, K_r , impacts the timescale of lesion development. The left plot depicts the time to steady state, defined numerically as the smallest time t for which $\sqrt{\sum_i (\frac{1}{y_i} \frac{dy_i}{dt})^2} \leq 10^{-8}$, where the sum is taken over all subsystem variables: $\mathbf{y} = (M, \hat{\Phi}_M, \hat{L}_M, H, L, S_{\pm})$. The time to steady state increases with K_r . The trend is more pronounced in the unhealthy case ($L^* = 4.5, H^* = 1$), which exhibits a 20-fold increase over $0.3 \leq K_r \leq 100$. The right plot shows the time, t_M , for MDM lipid to exceed 450mg/dL (the smallest t satisfying $(1 + \kappa \hat{L}_M(t))M(t) > 10$), which we use as a proxy for fatty streak onset. We find that increases to K_r yield smaller values of t_M ; regions with higher LDL retention capacity develop fatty streaks earlier. Moreover, if K_r is sufficiently small, the MDM lipid density never exceeds the 450mg/dL threshold; fatty streaks will not develop in regions of sufficiently low LDL retention capacity.

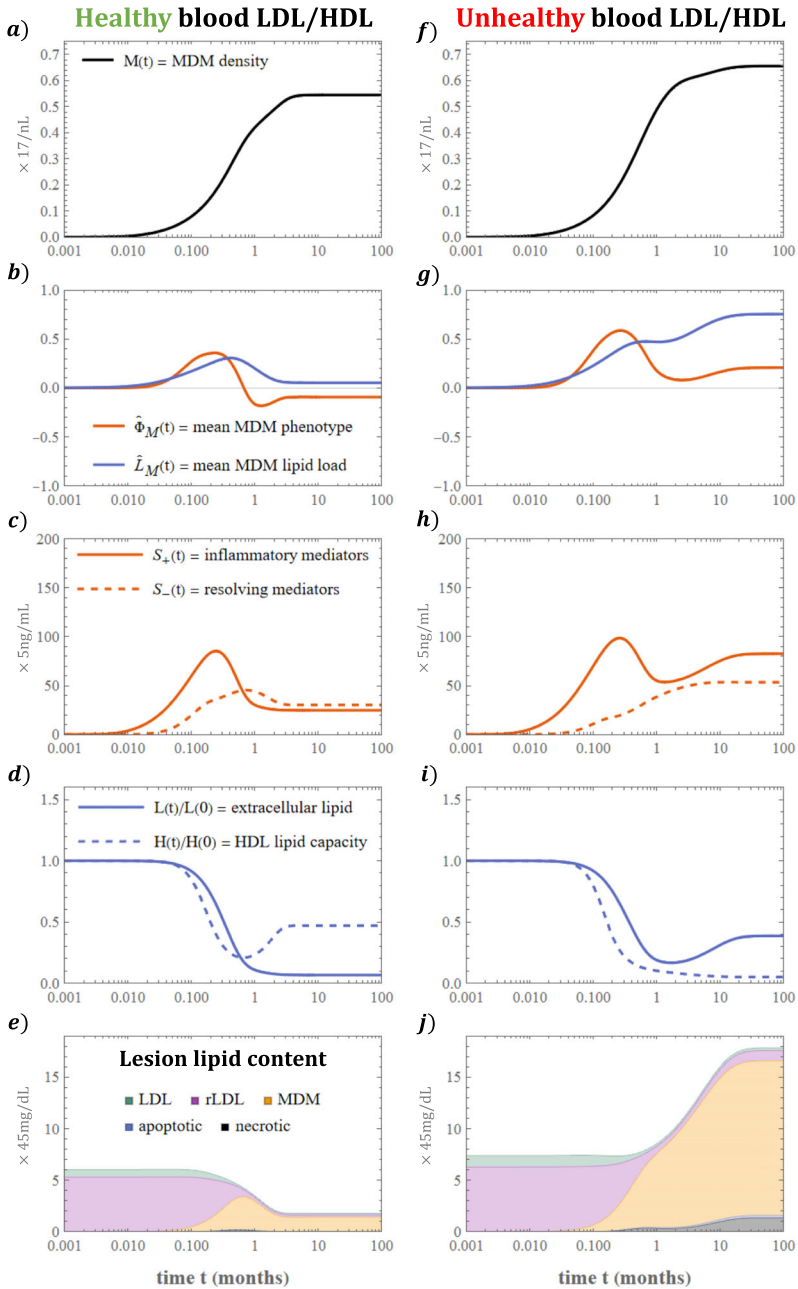


Fig. 3 Time evolution of lesion composition. The plots **a–j** show numerical solutions of the subsystem (32)–(41) for a case with healthy LDL–HDL balance: $L^* = 3$, $H^* = 2.5$ (left), and unhealthy LDL–HDL balance: $L^* = 4.5$, $H^* = 1$ (right). The system tends to a non-zero steady state as $t \rightarrow \infty$ with values that depend sensitively on L^* and H^* . We set $K_r = 10$ for both cases (Color figure online)

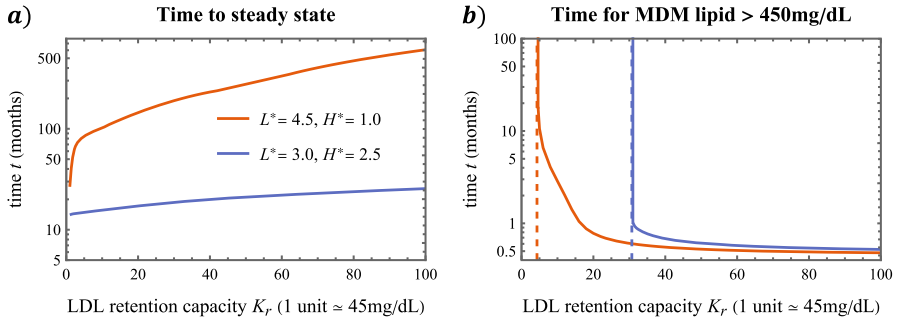


Fig. 4 LDL retention capacity modulates the timescale of lesion development. Plot **a** shows how time to steady state increases with K_r . Plot **b** shows how the time for MDM lipid to exceed 450mg/dL, a proxy for fatty streak onset, decreases with K_r (Color figure online)

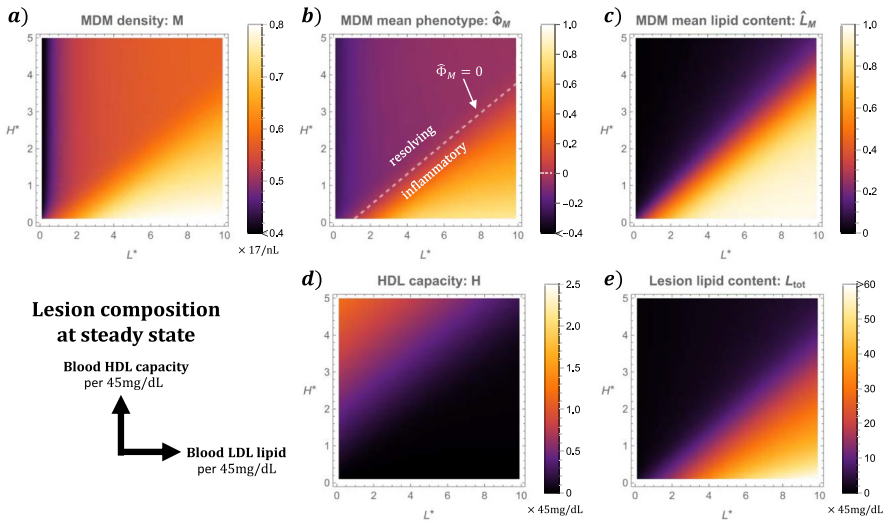


Fig. 5 Lesion composition at steady state depends on the bloodstream balance of LDL lipid (L^*) to HDL capacity (H^*). The plots depict solutions to Eqs. (32)–(41) at equilibrium across a uniform grid of values for (L^*, H^*). We use a grid resolution of 0.1 and assume $K_r = 10$. Note that the markers of pathology: $M, \hat{\Phi}_M, \hat{L}_M$ and L_{tot} , each increase with L^* and decrease with H^* (Color figure online)

3.1.2 Steady State Solutions

The results of Sect. 3.1.1 show that the model tends to a non-zero equilibrium as $t \rightarrow \infty$. Steady state solutions to the subsystem (32)–(41) are computed numerically via the Mathematica *FindRoot* routine.

Figure 5 illustrates how blood levels of LDL lipid, L^* , and HDL capacity, H^* , impact the model lesion at steady state. Lesion composition becomes more pathological as L^* increases and H^* decreases; MDM density, mean phenotype, lipid content and total lipid content each monotonically increase with L^* and decrease with H^* , while HDL capacity monotonically decreases with L^* and increases with H^* . We note

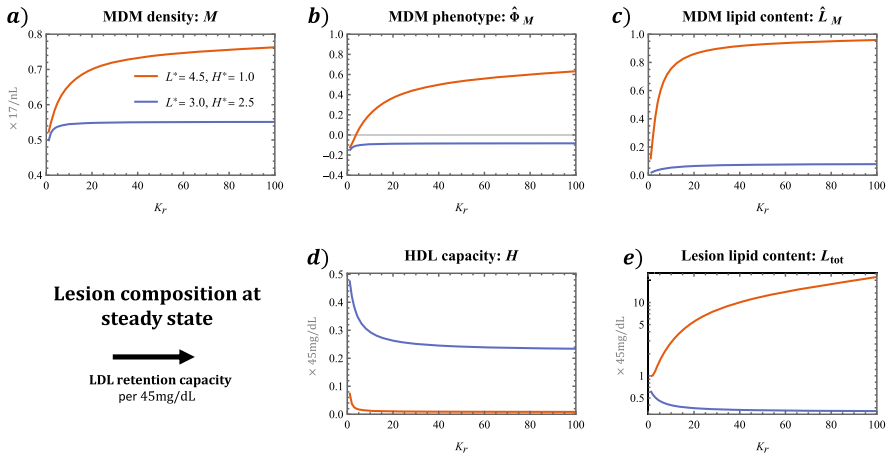


Fig. 6 Lesion composition at steady state varies with LDL retention capacity (K_r). The plots show solutions to Eqs. (32)–(41) at steady state across $0.3 \leq K_r \leq 100$. We show a case with healthy LDL–HDL balance: $L^* = 3.0$, $H^* = 2.5$, and one with unhealthy LDL–HDL balance: $L^* = 4.5$, $H^* = 1.0$ (Color figure online)

that all plots exhibit regions in which the contours are approximately linear. For the case $K_r = 10$ shown, these contours take the form $0.4L^* - H^* = \text{constant}$. The greater weighting on H^* in the linear combination reflects the higher value of the dimensionless lipid efflux rate, k_H , relative to the uptake rates in Table 2. Values of (L^*, H^*) above the $\hat{\phi}_M = 0$ contour ($0.4L^* - H^* \approx 0.4$) yield healthy lesions with smaller MDM densities, resolving mean phenotypes and small mean lipid loads. Lesion lipid content is low and HDL capacity remains substantial. Values of (L^*, H^*) below the $\hat{\phi}_M = 0$ contour yield pathological lesions with higher MDM densities, inflammatory mean phenotypes and higher mean lipid loads. Lesion lipid content is also large. These markers of pathology each increase with $0.4L^* - H^*$. By contrast the HDL capacity is exhausted in this region.

Figure 6 shows how the LDL retention capacity, K_r , impacts lesion composition at steady state. We find that MDM density, MDM mean phenotype and MDM lipid content increase non-linearly with K_r . These trends are amplified when the values (L^*, H^*) are more pathological (i.e. $0.4L^* - H^*$ is larger). HDL capacity instead decreases with K_r . Moreover, total lesion lipid content increases or decreases with K_r if the values (L^*, H^*) are pathological or healthy respectively. This difference arises because higher LDL retention capacities give rise to higher MDM densities, due partially to elevated signalling by resident cells. In healthy cases, HDL capacity remains substantial so that MDMs provide a net reduction in lesion lipid content by consuming extracellular lipid and efficiently offloading to HDL. In pathological cases, HDL capacity is exhausted and lipid taken up by MDMs can only leave the lesion via MDM egress. This makes MDMs net contributors to lesion lipid content; on average, they remove less lipid from the lesion than they supply via their endogenous lipid content.

3.2 MDM Phenotype-Lipid Distribution

We now turn to Eq. (29) to study how phenotype and lipid content are distributed amongst lesion MDMs. After presenting numerical solutions for $m_{\phi,\ell}(t)$ in Sect. 3.2.1, we derive a continuum approximation of Eq. (29) in Sect. 3.2.2 to make analytical progress. In Sect. 3.2.3 we show how analysis of the leading-order advective dynamics enables us to characterise the expected trajectories of MDMs through phenotype-lipid space. Finally, in Sect. 3.2.4 we analyse the MDM distribution at steady state.

3.2.1 Time Evolution

In Fig. 7 we present the dynamics of the MDM phenotype-lipid distribution, $m_{\phi,\ell}(t)$, for the cases shown in Fig. 3). At early times ($0 \leq t \leq 0.2$, the distribution evolves in a wave-like manner, from $(\phi, \ell) = (0, 0)$, in the direction of increasing ϕ and ℓ due to the initial phase of LDL uptake noted in Sect. 3.1.1. At later times ($0.2 \leq t \leq 2$), the distribution moves leftwards, becoming concentrated at lower values of ϕ . This resolving phenotype modulation reflects greater production of resolving mediators, S_- , relative to inflammatory mediators, S_+ , in this phase (c.f. Fig. 3e, h). At longer times, the distribution settles to a steady state. In the healthy case, lipid loads gradually reduce to equilibrium as HDL capacity increases and the extracellular lipid densities decrease to their equilibrium values (c.f. Fig. 3d, e). In the unhealthy case, lipid loads increase towards equilibrium as the extracellular lipid densities increase and HDL capacity declines to their steady state values (c.f. Fig. 3i, j).

We note that the MDM distribution, in both cases and at all times, is concentrated about a central curve which begins at the origin $(\phi, \ell) = (0, 0)$ and terminates at an interior point in (ϕ, ℓ) space. This feature indicates that phenotype and lipid content are non-linearly correlated. At steady state, this correlation is monotonic but may be negative (as in case a) or positive (as in case b) depending on model parameters.

It is not straightforward to understand how the MDM distributions in Fig. 7 arise by directly considering Eq. (29). In order to make progress, we consider a continuum approximation of Eq. (29) in the analysis below.

3.2.2 Continuum Approximation

We associate the discretely structured MDM distribution $m_{\phi,\ell}(t)$, $\phi = 0, \pm 1, \dots, \pm\phi_{\max}$, $\ell = 0, 1, \dots, \ell_{\max}$, with a function $m(\tilde{\phi}, \tilde{\ell}, t) \geq 0$ of two continuous structure variables, $\tilde{\phi}$ and $\tilde{\ell}$, and time t . Specifically, we make the identifications:

$$\tilde{\phi} \sim \frac{\phi}{\phi_{\max}}, \quad \tilde{\ell} \sim \frac{\ell}{\ell_{\max}}, \quad m(\tilde{\phi}, \tilde{\ell}, t) \sim \phi_{\max} \ell_{\max} m_{\phi,\ell}(t). \quad (47)$$

Here $\tilde{\phi} \in [-1, 1]$ and $\tilde{\ell} \in [0, 1]$, so that $\tilde{\phi} = -1$ corresponds to fully M2-polarised MDMs, $\tilde{\phi} = 1$ to fully M1-polarised MDMs, $\tilde{\ell} = 0$ to MDMs with only endogenous lipid, and $\tilde{\ell} = 1$ to MDMs at maximal lipid content. The function $m(\tilde{\phi}, \tilde{\ell}, t)$ can

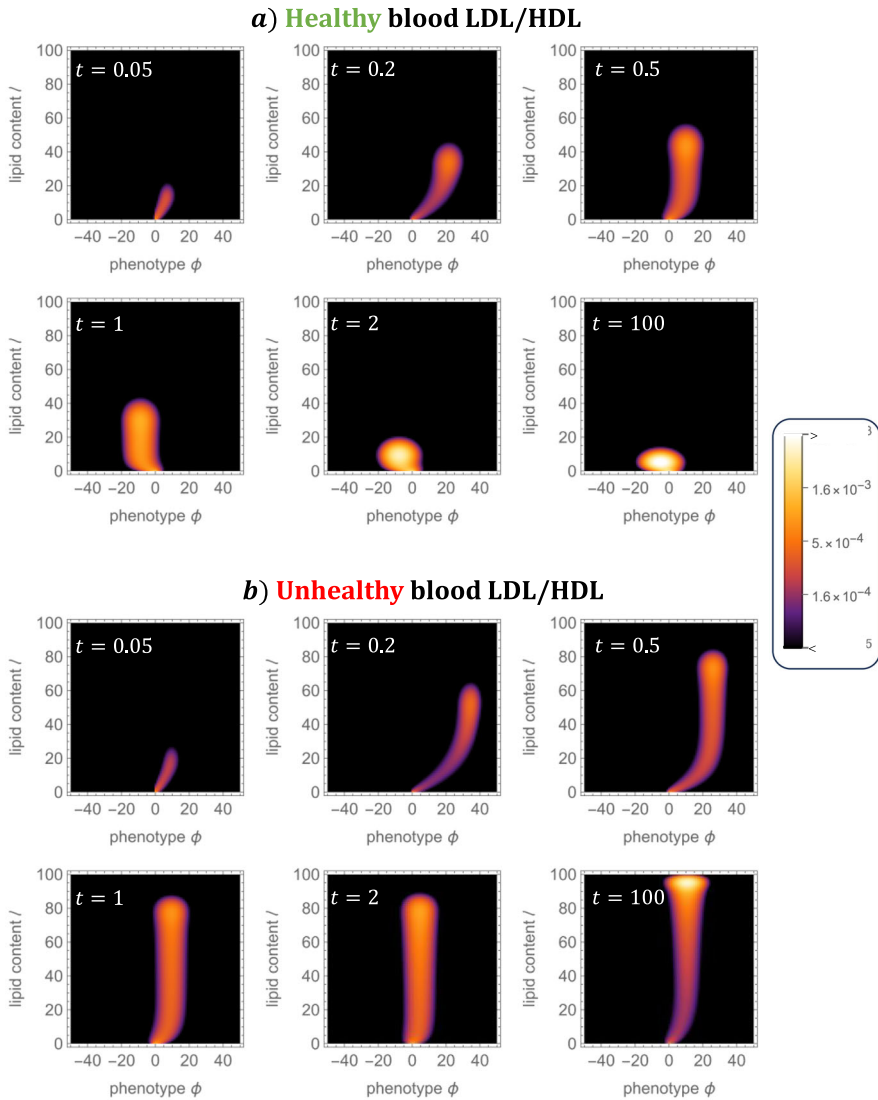


Fig. 7 MDM phenotype-lipid distribution dynamics for two typical simulations. The plots show numerical solutions of Eq. (29) for $m_{\phi, \ell}(t)$ for a case with healthy LDL/HDL balance. **a** $L^* = 3$, $H^* = 2.5$, and unhealthy LDL-HDL balance. **b** $L^* = 4.5$, $H^* = 1$. We use $K_r = 10$ for both simulations. At steady state (see $t = 100$), the distribution may skew towards resolving (case a) or inflammatory (case b) phenotypes (Color figure online)

be interpreted as the number density of MDMs across a continuous phenotype-lipid structure space, with scaling such that we may identify:

$$M(t) = \sum_{\phi, \ell} m_{\phi, \ell}(t) \sim \int_0^1 \int_{-1}^1 m(\tilde{\phi}, \tilde{\ell}, t) d\tilde{\phi} d\tilde{\ell}. \tag{48}$$

We seek an expansion of Eq. (29) in the limit $\ell_{\max} \sim \phi_{\max} \rightarrow \infty$. More precisely, we set $\epsilon := \ell_{\max}^{-1} \ll 1$ and assume that $\theta := \phi_{\max}/\ell_{\max} = \mathcal{O}(1)$. Substituting the identifications (47) into Eq. (29), Taylor-expanding about $\epsilon = 0$, and neglecting $\mathcal{O}(\epsilon^2)$ terms, yields the advection–diffusion PDE:

$$\frac{\partial m}{\partial t} = \nabla \cdot (\mathbf{D}\nabla m - \mathbf{v}m) - (1 + \gamma)m, \tag{49}$$

where $\nabla = \left(\frac{\partial}{\partial \tilde{\phi}}, \frac{\partial}{\partial \tilde{\ell}}\right)^T$, and the velocity vector, \mathbf{v} , and diffusivity matrix, \mathbf{D} , are respectively:

$$\mathbf{v} = \begin{bmatrix} \chi(S_+ - S_-) - \chi(S_+ + S_-)\tilde{\phi} \\ \mathbf{k}_L \cdot \mathbf{L} - (\mathbf{k}_L \cdot \mathbf{L} + k_H H)\tilde{\ell} \end{bmatrix} + \frac{\epsilon}{2} \begin{bmatrix} \theta\chi(S_+ - S_-) \\ \mathbf{k}_L \cdot \mathbf{L} - k_H H \end{bmatrix}, \tag{50}$$

$$\mathbf{D} = \frac{\epsilon}{2} \begin{bmatrix} \theta\chi[(S_+ + S_-) - (S_+ - S_-)\tilde{\phi}] & 0 \\ 0 & \mathbf{k}_L \cdot \mathbf{L} - (\mathbf{k}_L \cdot \mathbf{L} - k_H H)\tilde{\ell} \end{bmatrix}. \tag{51}$$

We note that Eq. (49) is advection-dominant since $\mathbf{v} = \mathcal{O}(1)$ and $\mathbf{D} = \mathcal{O}(\epsilon)$.

We derive boundary conditions for Eq. (49) by requiring that the dynamics of the MDM population, $M(t)$, as defined by Eq. (32), are consistent with those of the continuous MDM distribution (48). Integrating Eq. (49) over $(\tilde{\phi}, \tilde{\ell}) \in \mathcal{R} := [-1, 1] \times [0, 1]$ and applying the divergence theorem yields:

$$\frac{dM}{dt} = \oint_{\partial\mathcal{R}} (\mathbf{D}\nabla m - \mathbf{v}m) \cdot \mathbf{n} ds - (1 + \gamma)M, \tag{52}$$

where \mathbf{n} is the outwards pointing normal vector. We set:

$$(\mathbf{D}\nabla m - \mathbf{v}m) \cdot (\pm 1, 0)^T = 0 \quad \text{on } \tilde{\phi} = \pm 1, \tag{53}$$

$$(\mathbf{D}\nabla m - \mathbf{v}m) \cdot (0, +1)^T = 0 \quad \text{on } \tilde{\ell} = 1, \tag{54}$$

$$(\mathbf{D}\nabla m - \mathbf{v}m) \cdot (0, -1)^T = R_{0,0} \cdot \delta_0(\tilde{\phi}) \quad \text{on } \tilde{\ell} = 0. \tag{55}$$

Equations (53) and (54) are no-flux conditions so that MDMs cannot enter or leave the system by exceeding the phenotype bounds $\tilde{\phi} = \pm 1$ or maximal lipid content $\tilde{\ell} = 1$ respectively. We use the Dirac-delta distribution, δ_0 , in Eq. (55) to ensure that MDMs enter the lesion at the origin $(\tilde{\phi}, \tilde{\ell}) = (0, 0)$.

3.2.3 Advection at Leading Order

Equation (49) reduces to a hyperbolic PDE at leading order as $\epsilon \rightarrow 0$:

$$\begin{aligned} \frac{\partial m}{\partial t} + \chi \frac{\partial}{\partial \tilde{\phi}} \left[\left((S_+ - S_-) - (S_+ + S_-)\tilde{\phi} \right) m \right] \\ + \frac{\partial}{\partial \tilde{\ell}} \left[\left(\mathbf{k}_L \cdot \mathbf{L} - (\mathbf{k}_L \cdot \mathbf{L} + k_H H)\tilde{\ell} \right) m \right] = -(1 + \gamma)m. \end{aligned} \tag{56}$$

Eq. (56) describes the advection, in $(\tilde{\phi}, \tilde{\ell})$ space, of MDMs according to a time-dependent velocity field:

$$\frac{d\tilde{\phi}}{dt} = \chi[(S_+ - S_-) - (S_+ + S_-)\tilde{\phi}], \tag{57}$$

$$\frac{d\tilde{\ell}}{dt} = \mathbf{k}_L \cdot \mathbf{L} - (\mathbf{k}_L \cdot \mathbf{L} + k_H H)\tilde{\ell}, \tag{58}$$

where the coefficients: $S_{\pm}(t)$, $\mathbf{L}(t)$ and $H(t)$, are time-dependent solutions of the subsystem (32)–(41).

The dynamics of the velocity field defined by Eqs. (57)–(58) are illustrated in Fig. 8. A striking feature of the plots is that, at all times, the vector field has a single point $(\tilde{\phi}_\times, \tilde{\ell}_\times)$ of zero instantaneous velocity. This time-dependent point represents the target phenotype and lipid content that MDMs are driven towards by advection. Setting time derivatives to zero in Eqs. (57)–(58), and solving for $\tilde{\phi}$ and $\tilde{\ell}$ shows that:

$$\tilde{\phi}_\times(t) := \frac{S_+(t) - S_-(t)}{S_+(t) + S_-(t)}, \quad \tilde{\ell}_\times(t) := \frac{\mathbf{k}_L \cdot \mathbf{L}(t)}{\mathbf{k}_L \cdot \mathbf{L}(t) + k_H H(t)}. \tag{59}$$

The time-evolution of the zero velocity point, given by Eq. (59), is shown in Fig. 8c). We find that $(\tilde{\phi}_\times, \tilde{\ell}_\times)$ first moves from an inflammatory position towards resolving phenotypes. This initial transition occurs because resolving mediator production by MDMs opposes the initially pure inflammatory environment due to rLDL-stimulated resident cells. When the LDL/HDL balance is healthy, the target phenotype becomes resolving and the target lipid content decreases towards steady state. When the LDL/HDL balance is unhealthy, the target phenotype remains inflammatory and the target lipid content increases as the system evolves to its steady state. We note further that $(\tilde{\phi}_\times, \tilde{\ell}_\times)$ aligns well with the MDM distribution end points shown in Fig. 7.

Since MDMs enter the model lesion with minimal lipid content and a neutral phenotype, we are particularly interested in solutions to Eqs. (57)–(58) which satisfy the initial conditions:

$$\tilde{\phi}(t^*) = 0, \quad \tilde{\ell}(t^*) = 0. \tag{60}$$

Such solutions represent the trajectory of MDMs that enter the lesion at time $t = t^*$ in the limit $\epsilon \rightarrow 0$. They can be expressed in terms of the subsystem variables as follows:

$$\tilde{\phi}(t) = I_1(t)^{-1} \int_{t^*}^t \chi(S_+(\tau) - S_-(\tau))I_1(\tau)d\tau, \tag{61}$$

$$\tilde{\ell}(t) = I_2(t)^{-1} \int_{t^*}^t \mathbf{k}_L \cdot \mathbf{L}(\tau)I_2(\tau)d\tau, \quad t \geq t^*, \tag{62}$$

where $I_1(t)$ and $I_2(t)$ are integrating factors:

$$I_1(t) := e^{\int_{t^*}^t \chi(S_+(\tau)+S_-(\tau))d\tau}, \quad I_2(t) := e^{\int_{t^*}^t (\mathbf{k}_L \cdot \mathbf{L}(\tau)+k_H H(\tau))d\tau}.$$

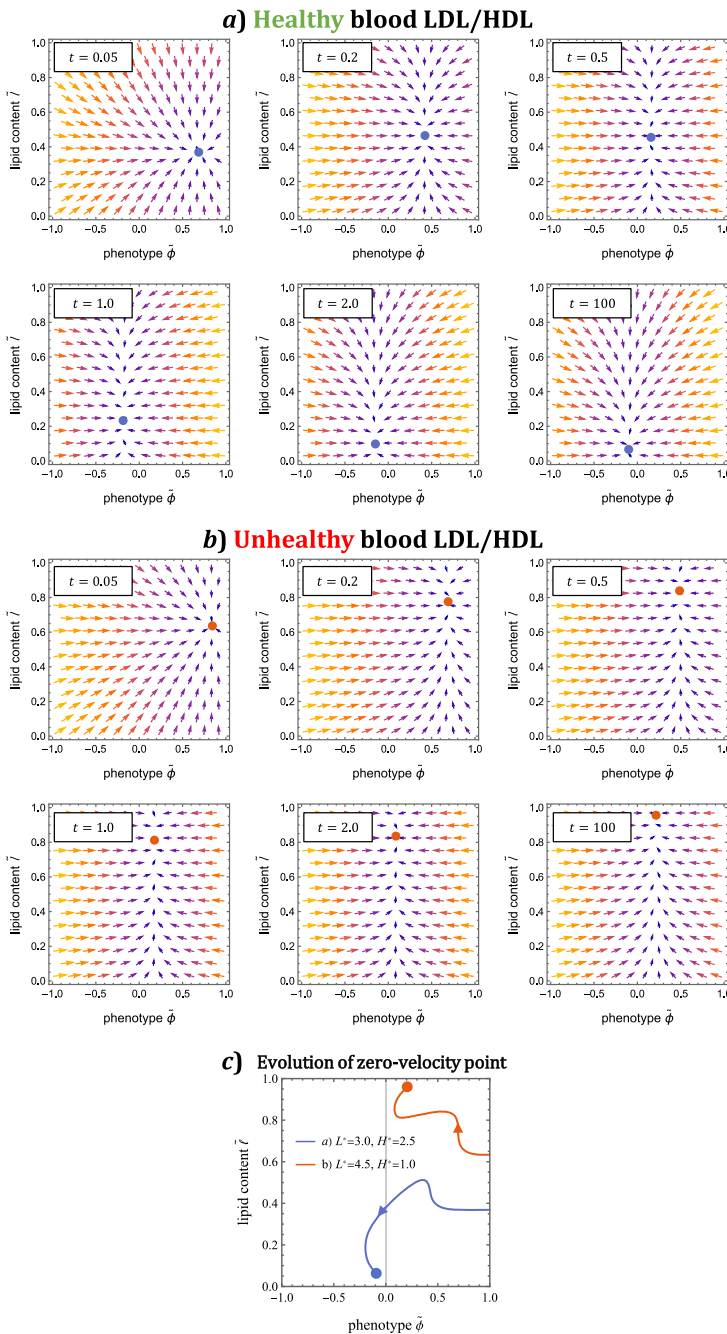


Fig. 8 Dynamics of the MDM phenotype-lipid velocity field. The vector field plots illustrate the right hand side of Eqs. (57)–(58) using the numerical solutions of the subsystem (32)–(41) shown in Fig. 3. The velocity magnitude is indicated by larger arrows and brighter colours. The point of instantaneous zero velocity is indicated by a circle at each time point in the vector field plots, and plotted against time in the bottom plot. We fix $K_T = 10$ and use $L^* = 4.5, H^* = 1.0$ for case a) and $L^* = 3.0, H^* = 2.5$ for case b) (Color figure online)

Expected MDM trajectories

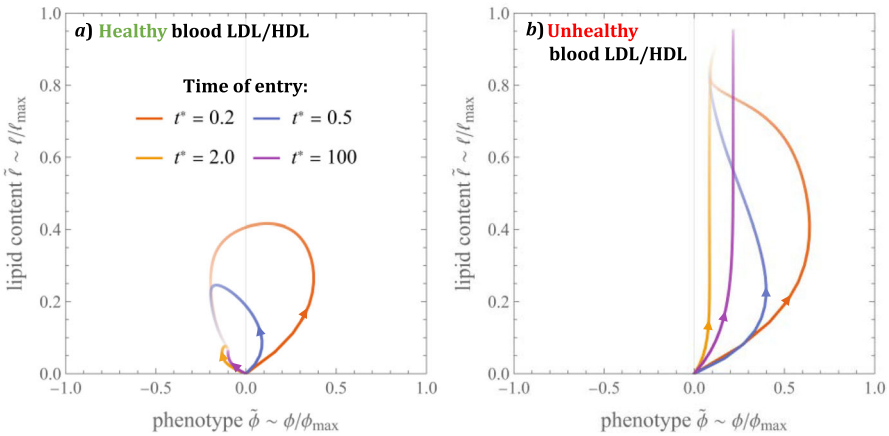


Fig. 9 Expected trajectory through phenotype-lipid content space of MDMs that enter the lesion at time $t = t^*$. The curves are numerical solutions to Eqs. (57)–(60). The opacity of each point on the curves represents the probability that MDMs travel through that point before either dying or emigrating from the lesion. Note how MDMs which enter at later times have simple monotonic trajectories, in contrast to those that enter earlier (Color figure online)

We use numerical solutions of the subsystem (32)–(44) to evaluate Eqs. (61)–(62) in Fig. 9. As MDMs travel along the trajectories shown, they emigrate from the lesion and die via apoptosis at the constant rate $(1 + \gamma)$. The probability that MDMs which enter the lesion at time $t = t^*$ are still alive and in the lesion at time $t \geq t^*$ is given by $e^{-(1+\gamma)(t-t^*)}$. This probability is represented in Fig. 9 by the opacity of the curves. The plots illustrate that MDMs which enter the lesion early (e.g. at $t^* = 0.2$) can be expected to first transition from phenotypic neutrality to an inflammatory state with moderate lipid loads, before evolving to either a resolving phenotype with low lipid load (case a), or a milder inflammatory phenotype with high lipid load (case b). The trajectories of MDMs that enter the lesion at later times are typically monotonic, in contrast to the looping trajectories of MDMs that enter at earlier times. We note in particular that trajectories with $t^* = 100$ (near steady state) align well with the centre line of the MDM distributions (c.f. Fig. 7 at $t = 100$).

3.2.4 Steady State Solutions

It is straightforward to show that $m^*(\tilde{\phi}, \tilde{\ell})$, the steady state solution of Eq. (49), satisfies:

$$\begin{aligned} & \frac{\epsilon \theta q}{2} \frac{\partial^2}{\partial \tilde{\phi}^2} \left[(1 - \tilde{\phi}_\infty \tilde{\phi}) m^* \right] + \frac{\epsilon}{2} \frac{\partial^2}{\partial \tilde{\ell}^2} \left[(\tilde{\ell}_\infty - (2\tilde{\ell}_\infty - 1)\tilde{\ell}) m^* \right] \\ & - q(\tilde{\phi}_\infty - \tilde{\phi}) \frac{\partial m^*}{\partial \tilde{\phi}} - (\tilde{\ell}_\infty - \tilde{\ell}) \frac{\partial m^*}{\partial \tilde{\ell}} - (p - q)m^* = 0, \end{aligned} \tag{63}$$

where the constants $\tilde{\phi}_\infty, \tilde{\ell}_\infty, q$ and p are defined in terms of model parameters and the equilibrium values of the subsystem variables:

$$\begin{aligned} \tilde{\phi}_\infty &:= \frac{S_+ - S_-}{S_+ + S_-}, & \tilde{\ell}_\infty &:= \frac{\mathbf{k}_L \cdot \mathbf{L}}{\mathbf{k}_L \cdot \mathbf{L} + k_H H}, \\ q &:= \frac{\chi(S_+ + S_-)}{\mathbf{k}_L \cdot \mathbf{L} + k_H H}, & p &:= -1 + \frac{1 + \gamma}{\mathbf{k}_L \cdot \mathbf{L} + k_H H}. \end{aligned} \tag{64}$$

We note that $\tilde{\phi}_\infty \in (-1, 1)$ and $\tilde{\ell}_\infty \in (0, 1)$ coincide exactly with the target phenotype and lipid content, $\tilde{\phi}_\times$ and $\tilde{\ell}_\times$ respectively (c.f. Eq. (59) at steady state). We note also that $p \in (-1, \infty)$ and $q \in (0, \infty)$. The boundary conditions (53)–(55) become:

$$J_\phi|_{\tilde{\phi}=-1} = 0, \quad J_\phi|_{\tilde{\phi}=1} = 0, \quad J_\ell|_{\tilde{\ell}=1} = 0, \quad J_\ell|_{\tilde{\ell}=0} = \left(\frac{\tilde{\ell}_\infty R_{0,0}}{\mathbf{k}_L \cdot \mathbf{L}}\right) \cdot \delta_0(\tilde{\phi}), \tag{65}$$

where the dimensionless fluxes are given by:

$$J_\phi = q(\tilde{\phi}_\infty - \tilde{\phi})m^* - \frac{\epsilon\theta q}{2} \frac{\partial}{\partial \tilde{\phi}} \left[(1 - \tilde{\phi}_\infty \tilde{\phi})m^* \right], \tag{66}$$

$$J_\ell = (\tilde{\ell}_\infty - \tilde{\ell})m^* - \frac{\epsilon}{2} \frac{\partial}{\partial \tilde{\ell}} \left[(\tilde{\ell}_\infty - (2\tilde{\ell}_\infty - 1)\tilde{\ell})m^* \right]. \tag{67}$$

Rather than searching for a closed-form solutions to Eq. (63) in full generality, we characterise the solutions via asymptotic analysis in the limit $\epsilon \rightarrow 0$. More specifically, we derive equations for the central curve of the MDM distribution and marginal distributions with respect to lipid content, $W(\tilde{\ell})$, and phenotype, $V(\tilde{\phi})$, where:

$$W(\tilde{\ell}) := \int_{-1}^1 m^*(\tilde{\phi}, \tilde{\ell}) d\tilde{\phi}, \quad V(\tilde{\phi}) := \int_0^1 m^*(\tilde{\phi}, \tilde{\ell}) d\tilde{\ell}. \tag{68}$$

Finally, we consider the impact of the LDL lipid and HDL capacity blood densities, L^* and H^* respectively. The results are summarised in Figs. 10 and 11.

Central curve We determine the curve about which $m^*(\tilde{\phi}, \tilde{\ell})$ is centred by considering Eq. (63) at leading order. Indeed, when $\epsilon = 0$, Eq. (63) reduces to a first order hyperbolic PDE, with characteristics that satisfy the equation:

$$\frac{d\tilde{\phi}}{d\tilde{\ell}} = \frac{q(\tilde{\phi}_\infty - \tilde{\phi})}{\tilde{\ell}_\infty - \tilde{\ell}}. \tag{69}$$

Solving Eq. (69) subject to $\tilde{\phi}(\tilde{\ell} = 0) = 0$ yields:

$$\tilde{\phi} = \tilde{\phi}_c(\tilde{\ell}) := \tilde{\phi}_\infty \left[1 - \left(1 - \frac{\tilde{\ell}}{\tilde{\ell}_\infty} \right)^q \right]. \tag{70}$$

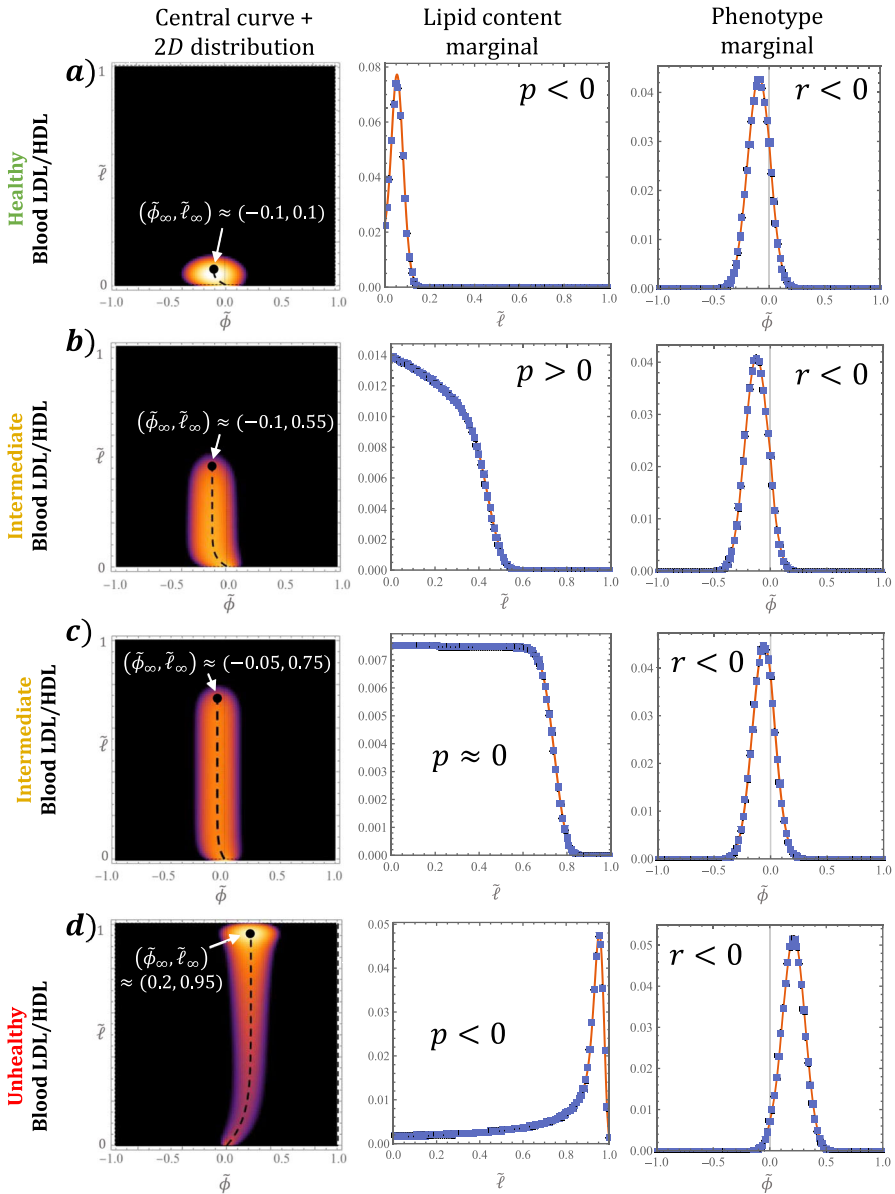


Fig. 10 Comparison of continuum analytical results to numerical solutions for the discrete MDM distribution, $m_{\phi, \ell}$, at steady state. Cases **a–d** use the values $(L^*, H^*) = (3, 2.5), (1.7, 0.8), (1.9, 0.6)$ and $(4.5, 1)$ and are ordered roughly by pathology. The first column overlays Eq. (70) for the central curve with $m_{\phi, \ell}$ (same colour legend as in Fig. 7). The second and third columns compare the exact solutions for the lipid content and phenotype marginals, given by Eqs. (73) and (83) respectively, with the discrete marginals. We set $K_T = 10$ for all cases (Color figure online)

In the first column of Fig. 10, the solution (70) is superimposed on numerical solutions for $m_{\phi,\ell}$ at steady state, showing good agreement with the centre of the MDM distributions.

Equation (70) confirms that, at steady state, phenotype and lipid content are monotonically correlated via a power law. The correlation is positive when $\tilde{\phi}_\infty > 0$ and negative when $\tilde{\phi}_\infty < 0$. Equivalently, using the first of Eqs. (64), if inflammatory mediators dominate resolving ones ($S_+ > S_-$) then MDMs with higher lipid loads have a more inflammatory phenotype; if, however, resolving mediators dominate ($S_+ > S_-$) then MDMs with higher lipid loads have a more resolving phenotype. The nonlinearity of the correlation is determined by the constant q , which measures the relative amount of mediator-MDM activity to lipid-MDM activity.

Distribution of lipid content Integrating Eqs. (63) and (65) with respect to $\tilde{\phi} \in [-1, 1]$ yields the following ODE for $W(\tilde{\ell})$:

$$\frac{\epsilon}{2} \frac{d^2}{d\tilde{\ell}^2} [(\tilde{\ell}_\infty - (2\tilde{\ell}_\infty - 1)\tilde{\ell})W] - (\tilde{\ell}_\infty - \tilde{\ell}) \frac{dW}{d\tilde{\ell}} - pW = 0, \tag{71}$$

and the boundary conditions:

$$-\frac{\epsilon}{2} \frac{d}{d\tilde{\ell}} [(\tilde{\ell}_\infty - (2\tilde{\ell}_\infty - 1)\tilde{\ell})W] + (\tilde{\ell}_\infty - \tilde{\ell})W = \begin{cases} \frac{\tilde{\ell}_\infty R_{0,0}}{k_L \cdot L} & \text{at } \tilde{\ell} = 0, \\ 0 & \text{at } \tilde{\ell} = 1. \end{cases} \tag{72}$$

Equation (71) admits an exact solution (found via the Mathematica *DSolve* routine):

$$W(\tilde{\ell}) = e^{-f(\tilde{\ell})} \left[K_1 U_p^{2-f(\tilde{\ell}_\infty)}(f(\tilde{\ell})) + K_2 \mathcal{L}_{-p}^{1-f(\tilde{\ell}_\infty)}(f(\tilde{\ell})) \right], \tag{73}$$

where f is the function:

$$f(\tilde{\ell}) := \frac{2}{(1 - 2\tilde{\ell}_\infty)\epsilon} \left[\tilde{\ell} + \left(\frac{\tilde{\ell}_\infty}{1 - 2\tilde{\ell}_\infty} \right) \right], \tag{74}$$

$U_a^b(z)$ is the confluent hypergeometric function and $\mathcal{L}_a^b(z)$ the generalised Laguerre polynomial. The constants K_1 and K_2 are determined by substituting Eq. (73) into the boundary conditions (72); exact expressions are readily obtained via the Mathematica *Solve* routine, but are too involved to be insightful and so are omitted here for brevity. We compare the solution (73) to numerical solutions of the discrete model in the second column of Fig. 10, showing excellent agreement.

The form of Eq. (73) makes it difficult to understand how $W(\tilde{\ell})$ depends on the constants defined in Eq. (64). Nonetheless, analysis of the leading order “outer” solution shows how the qualitative behaviour of $W(\tilde{\ell})$ depends on p and $\tilde{\ell}_\infty$. Here we follow the asymptotic analysis in Chambers et al. (2023). Setting $\epsilon = 0$ in Eq. (71) admits the following solution:

$$W_{\text{outer}}(\tilde{\ell}) = K_3 \left(1 - \frac{\tilde{\ell}}{\tilde{\ell}_\infty} \right)^p, \tag{75}$$

where $K_3 \geq 0$ is a constant of integration. Equation (75) admits three possible behaviours as $\tilde{\ell} \rightarrow \tilde{\ell}_\infty$ from below. For $p > 0$, W_{outer} decreases monotonically to zero (with non-zero derivative if $p < 2$); for $p = 0$, W_{outer} is constant; and for $p < 0$, W_{outer} diverges to $+\infty$. The full solution does not exhibit such discontinuities at $\tilde{\ell} = \tilde{\ell}_\infty$ due to the regularising effects of the second derivative term. The corresponding behaviour for $W(\tilde{\ell})$ is as follows. For $p > 0$, W decreases monotonically and smoothly to zero near $\tilde{\ell} = \tilde{\ell}_\infty$ (Fig. 10b); for $p = 0$, W takes a quasi-uniform sigmoidal profile with a rapid decrease to zero near $\tilde{\ell} = \tilde{\ell}_\infty$ (Fig. 10c); and for $p < 0$, W increases monotonically before attaining a local maximum near $\tilde{\ell} = \tilde{\ell}_\infty$ (Fig. 10a, d). In the above, “near $\tilde{\ell} = \tilde{\ell}_\infty$ ” means an $\mathcal{O}(\epsilon^{\frac{1}{2}})$ neighbourhood of $\tilde{\ell} = \tilde{\ell}_\infty$. This scaling can be derived by searching for an inner variable $\hat{\ell} = (\tilde{\ell} - \tilde{\ell}_\infty)/\epsilon^n$ for some $\hat{\ell} = \mathcal{O}(1)$ in Eq. (71); an exponent $n = \frac{1}{2}$ is required to bring the second derivative into the dominant balance.

Distribution of phenotype Integrating Eqs. (63) and (65) with respect to $\tilde{\ell} \in [0, 1]$ gives the following boundary value problem for $V(\tilde{\phi})$:

$$\frac{\epsilon\theta}{2} \frac{d^2}{d\tilde{\phi}^2} [(1 - \tilde{\phi}_\infty\tilde{\phi})V] - (\tilde{\phi}_\infty - \tilde{\phi}) \frac{dV}{d\tilde{\phi}} - rV = -\frac{\tilde{\ell}_\infty R_{0,0}}{q\mathbf{k}_L \cdot \mathbf{L}} \cdot \delta_0(\tilde{\phi}), \tag{76}$$

$$-\frac{\epsilon\theta}{2} \frac{\partial}{\partial \tilde{\phi}} [(1 - \tilde{\phi}_\infty\tilde{\phi})V] + (\tilde{\phi}_\infty - \tilde{\phi})V = 0 \quad \text{at } \tilde{\phi} = \pm 1, \tag{77}$$

where $r := -1 + \frac{p+1}{q}$. As in the derivation of a Green’s function, we first recast the Dirac-delta source, which describes MDM recruitment, as a jump condition. That is, we seek a solution of the form:

$$V(\tilde{\phi}) = \begin{cases} V_-(\tilde{\phi}), & -1 \leq \tilde{\phi} \leq 0; \\ V_+(\tilde{\phi}), & 0 \leq \tilde{\phi} \leq 1, \end{cases} \tag{78}$$

where V_\pm solve the ODE:

$$\frac{\epsilon\theta}{2} \frac{d^2}{d\tilde{\phi}^2} [(1 - \tilde{\phi}_\infty\tilde{\phi})V_\pm] - (\tilde{\phi}_\infty - \tilde{\phi}) \frac{dV_\pm}{d\tilde{\phi}} - rV_\pm = 0, \tag{79}$$

and satisfy:

$$V_-(0) = V_+(0) \tag{80}$$

$$V'_-(0) = V'_+(0) + \frac{2\tilde{\ell}_\infty R_{0,0}}{\epsilon\theta q\mathbf{k}_L \cdot \mathbf{L}} \tag{81}$$

$$-\frac{\epsilon\theta}{2} [(1 - \tilde{\phi}_\infty\tilde{\phi})V_\pm]' + (\tilde{\phi}_\infty - \tilde{\phi})V_\pm = 0 \quad \text{at } \tilde{\phi} = \pm 1. \tag{82}$$

The exact solution for Eq. (79) can be written as:

$$V_\pm(\tilde{\phi}) = J_{\pm,1} U_{-r}^{1+g(\tilde{\phi}_\infty)}(g(\tilde{\phi})) + J_{\pm,2} \mathcal{L}_r^{g(\tilde{\phi}_\infty)}(g(\tilde{\phi})), \tag{83}$$

where:

$$g(\tilde{\phi}) := \frac{2(\tilde{\phi}_\infty \tilde{\phi} - 1)}{\epsilon \theta \tilde{\phi}_\infty^2}. \tag{84}$$

Expressions for the constants $J_{\pm,1}$, $J_{\pm,2}$ can be found by substituting Eq. (83) into conditions (80)–(82). As for $W(\tilde{\ell})$, they are too complicated to be insightful and are omitted for brevity. The comparison of solutions (83) with the discrete model output in column 3 of Fig. 10 shows good agreement. We note that the jump condition amounts to a small reduction in slope at $\tilde{\phi} = 0$ that is almost imperceptible for the parameter values in Table 1.

Following the analysis of $W(\tilde{\ell})$, we compute the leading order “outer” solution to Eq. (76):

$$V_{\text{outer}} = J_3 \left(1 - \frac{\tilde{\phi}}{\tilde{\phi}_\infty} \right)^r. \tag{85}$$

Equation (85) is of the same form as Eq. (75); $\tilde{\phi}_\infty$ and r play the same roles for V as $\tilde{\ell}_\infty$ and p play for W . The main difference, as shown in Fig. 10, is that only the case $r < 0$ manifests in numerical solutions. Consequently, $V(\tilde{\phi})$ always attains a local maximum in a small (again $\mathcal{O}(\epsilon^{\frac{1}{2}})$) neighbourhood of $\tilde{\phi} = \tilde{\phi}_\infty$. This observation is supported by the numerical results below.

Impact of blood LDL lipid and HDL capacity levels. We conclude our steady state analysis by examining how the qualitative form of the MDM distribution changes as L^* and H^* vary. The results are summarised in Fig. 11 where we plot the parameter groupings in Eqs. (64) against L^* and H^* ; the four cases shown in Fig. 10 are also indicated. Recall that p and r determine the overall shape (e.g. whether they attain a local maximum) of the lipid and phenotype marginal distributions, $W(\tilde{\ell})$ and $V(\tilde{\phi})$ respectively, while $\tilde{\phi}_\infty$, $\tilde{\ell}_\infty$ and q determine the central curve.

We note first how r and p vary with L^* and H^* . The value of r decreases monotonically with L^* and is less sensitive to H^* . Importantly, we find that $r < 0$ for all $L^* \in (0, 10)$ and $H^* \in (0, 5)$, indicating that the phenotype marginal attains a local maximum near $\tilde{\phi} = \tilde{\phi}_\infty$ across the range of physiologically plausible values for blood LDL lipid and HDL capacity. By contrast, $p \geq 0$ for values of (L^*, H^*) sufficiently close to the origin. This suggests that monotone decreasing and sigmoidal lipid marginals only occur when blood levels of LDL lipid and HDL capacity are both sufficiently low; otherwise the lipid marginal attains a local maximum near $\tilde{\ell} = \tilde{\ell}_\infty$.

The target phenotype, $\tilde{\phi}_\infty$, and lipid content, $\tilde{\ell}_\infty$, both increase with L^* and decrease with H^* . In particular, their plots exhibit the linear contours prominent in Fig. 5; increases to the relative level of LDL lipid to HDL capacity raise both these markers of pathology.

Finally, we note that the exponent q of the central curve is largest when L^* and H^* are comparable. This causes the central curve to appear straighter (i.e. $\tilde{\phi}_c(\tilde{\ell}) \approx \tilde{\phi}_\infty$) except for the smallest values of $\tilde{\ell}$ in cases of intermediate pathology. Indeed, in

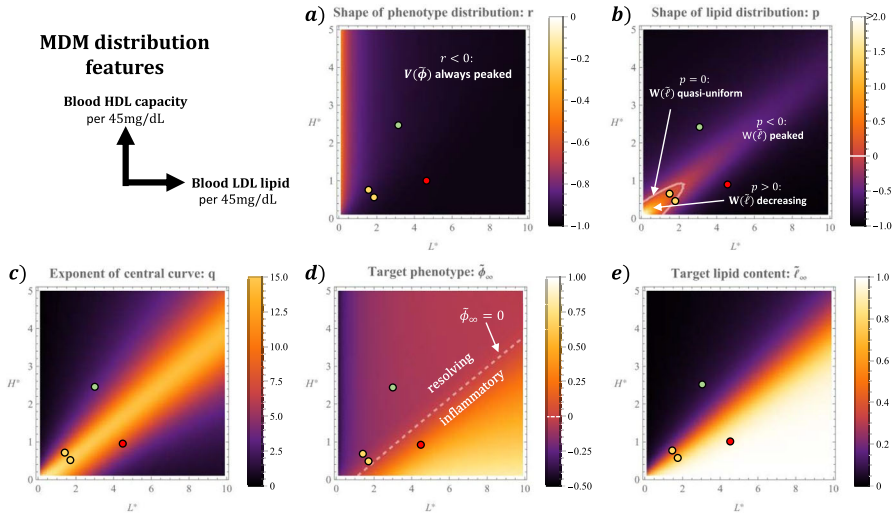


Fig. 11 Impact of blood LDL lipid (L^*) and HDL capacity (H^*) on the qualitative features of the MDM distribution. The values were computed by combining the results shown in Fig. 5 with the formulae (64) and $r = -1 + \frac{p+1}{q}$. The four cases presented in Fig. 10 are also indicated: $(L^*, H^*) = (3, 2.5), (1.7, 0.8), (1.9, 0.6)$ and $(4.5, 1)$ (Color figure online)

Fig. 10 the intermediate cases b) and c) are notably straighter than the unhealthy case d).

4 Discussion

In this paper we have developed a mathematical model for early atherosclerosis in which the MDM population is structured by phenotype, ϕ , and lipid content, ℓ . This framework allows for incremental changes in phenotype and lipid content, which contrasts their treatment as binary variables in much of the existing modelling literature. The model couples the MDM dynamics to the densities of: free LDL lipid $L_{LDL}(t)$, retained LDL lipid $L_r(t)$, apoptotic lipid, $L_{ap}(t)$, necrotic lipid, $L_n(t)$, HDL capacity, $H(t)$, inflammatory mediators, $S_+(t)$, and resolving mediators, $S_-(t)$. These variables form a closed subsystem of ODEs when coupled with the MDM density, $M(t)$, mean phenotype, $\hat{\Phi}_M(t)$, and mean lipid content, $\hat{L}_M(t)$. This subsystem can be solved independently of the structured MDM population, $m_{\phi,\ell}(t)$.

We parameterised the model using data from the biological literature. Where possible, we used human *in vivo* data (e.g. blood measurements for $L^{(0)}$ and $H^{(0)}$) or *ex vivo* data (e.g. surgical data for $\pi_L^{(0)}$ and postmortem data for $L^{(1)}$ and $H^{(1)}$). However, the majority of the model parameters are calibrated to *in vitro* experiments. We prioritised studies with human cell lines (e.g. for $a_0, k_{LDL}, k_r, k_H, S_+^{c50}, \rho$), and used data from nonhuman cell lines when necessary (e.g. murine data for κ, k_{ap} and k_n). Since the point estimates in Table 1 are likely to carry high degrees of uncertainty,

we have cautiously interpreted the results of the current study by focusing on trends rather than precise quantitative outputs.

Our model analysis focused on the impact of three dimensionless parameters: L^* , H^* and K_r . The quantities L^* and H^* are proportional to the blood densities of LDL lipid and HDL capacity, respectively. These vary considerably according to genetic and lifestyle factors. We explored values in the range $L^* \in (0, 10)$ and $H^* \in (0, 5)$; the upper bounds correspond to densities of 450 and 225mg/dL, respectively. The quantity K_r is proportional to the capacity for LDL lipid retention. This varies according to the specific region of artery wall under consideration. We explored values $K_r \in (0.3, 100)$, which span athero-resistant regions with capacity 15mg/dL to athero-prone regions with capacity 7500 mg/dL.

We discuss our findings below in relation to the key questions posed in Sect. 1.

Q1.a. How do blood LDL/HDL levels affect the time-evolution of lesion composition? Time-dependent numerical solutions revealed that the model lesion evolves in three phases. The first phase consists of the initial influx of MDMs and corresponding decline in lesion LDL and rLDL content. MDM lipid loads are small but increasing and MDM mean phenotype is inflammatory. The second phase is characterised by modulation towards resolving MDM phenotypes and a slower rise of MDM lipid content. These phases are consistent with observations of macrophage behaviour during acute inflammation. Macrophages first adopt inflammatory phenotypes and transition to resolving phenotypes during a phase of inflammatory resolution and tissue repair (Pérez and Rius-Pérez 2022). To the best of our knowledge, the present model is the first to capture this transition as an emergent property of the dynamics. Rather than completely resolving, however, the model lesion enters a final phase in which the dynamics tend to a nonzero steady state. If blood LDL lipid is low relative to HDL capacity, the lesion tends to a healthy state with low lipid burden and resolving phenotypes. This behaviour suggests that the well-documented spontaneous regression of many early atherosclerotic lesions (Insull 2009) may simply be the natural and expected progression under a healthy blood lipoprotein balance. By contrast, when blood LDL lipid is high relative to HDL capacity, MDM lipid loads increase to equilibrium and the model lesion accumulates necrotic lipid. Overall, the three-phase dynamics support the idea that chronic inflammation in atherosclerosis can be understood as an acute inflammatory response to LDL retention with incomplete resolution (Sansbury and Spite 2016).

We also studied the impact of LDL retention capacity on the timescale of atherosclerosis development. In particular, we computed the time for MDM lipid to exceed a density of 450mg/dL; we use this lipid density as a proxy for fatty streak formation, which is characterised by the appearance of foam cells (Daskalopoulos et al. 2015). Our results indicate that this time decreases with LDL retention capacity; fatty streak onset in the model lesion occurs earlier for regions of high LDL retention. This finding is consistent with observations of the murine aortic arch in which regions of lower retention capacity (e.g. central zone of the arch) developed atherosclerosis later than regions of high retention (e.g. dorsal and ventral zones) (Lewis et al. 2023).

Q1.b. How do blood LDL/HDL levels affect lesion composition at steady state? Analysis of steady state solutions revealed how equilibrium lesion composition depends on the parameters L^* , H^* and K_r . The results indicate that the degree of

pathology is largely determined by a linear combination of the form: $0.4L^* - H^*$; it is the (weighted) *relative* value of LDL lipid to HDL capacity in the blood that matters. The greater weighting on H^* in the linear combination reflects the higher value of the dimensionless lipid efflux rate, k_H , relative to the uptake rates in Table 2. Hence, the increased amount of lipid efflux promoted by a rise in blood HDL lipid capacity is greater than the increase in lesion lipid content by an equal rise in blood LDL lipid density. Overall, the model predicts that early atherosclerotic lesions regress upon blood LDL lipid density increases or blood HDL capacity increases. The degree of pathology also generally increases with K_r . Regions of higher LDL retention capacity exhibit greater MDM densities, more inflammatory MDM phenotypes and higher MDM lipid loads.

Q2.a. How do MDM phenotype and lipid content evolve over time? We analysed the MDM distribution by deriving a continuum analogue of the discrete equations (29) for $m_{\phi, \ell}(t)$. Analysis of the continuum model showed that the time-evolution of phenotype and lipid content for individual MDMs depends on the time of entry into the lesion. MDMs which enter the lesion at early times are expected to first transition from phenotypic neutrality to an inflammatory state, and then to a resolving state (if the blood LDL–HDL balance is healthy) or to a milder inflammatory state (if the LDL–HDL balance is unhealthy). The trajectories of MDMs which enter the lesion at later times are monotonic (in phenotype–lipid structure space) and follow the central curve of the equilibrium MDM distribution. These results suggest that MDMs which enter the lesion during early stages of lesion development experience a greater amount of phenotype modulation throughout their lifespan than those entering at later times.

Q2.b. Are MDM phenotype and lipid content correlated? The asymptotic analysis presented in Sect. 3.2.4 showed that MDM phenotype and lipid content are correlated via a power law at steady state. If LDL lipid density dominates HDL capacity in the blood, lipid-laden MDMs have a more inflammatory phenotype than lipid-poor MDMs, while if blood LDL lipid density is sufficiently low, lipid-laden MDMs have a more resolving phenotype than MDMs with a lower lipid burden. The non-linearity of the correlation is determined by a constant, q , that measures the relative amount of lipid activity to mediator activity in the lesion (made precise by Eq. (64)). Although we did not pursue a time-dependent mathematical analysis, numerical solutions (e.g. Figure 7) demonstrated that the MDM phenotype–lipid distribution is always concentrated about a central curve, indicating that a monotone correlation between phenotype and lipid content holds for all times. These findings are consistent with the recent discovery of PLIN2^{hi}/TREM1^{hi} macrophages in human lesions, for which the transcriptional signatures of lipid loading and inflammation are coupled (Dib et al. 2023).

Q2.c. What are the qualitative features of the phenotype and lipid content marginal distributions at steady state? Further analysis in Sect. 3.2.4 showed that the phenotype marginal distribution always attains a single local maximum. The location of the maximum, which represents the most common phenotype in the lesion, is a close approximation to the “target” phenotype that MDMs are driven towards by the extracellular environment over their lifetime. By contrast, the lipid marginal distribution varies more in shape as L^* and H^* are varied; it may exhibit a local maximum, adopt a quasi-uniform profile, or decrease monotonically according to the value of p , a constant which quantifies the amount of MDM–lipid activity in the lesion.

Future directions and conclusions There is considerable scope to extend our model. In the present model, phenotype influences the MDM dynamics via its impact on mediator production; macrophage phenotype is largely characterised by the profile of cytokines/effector molecules produced by the cell (Brown et al. 2009). In practice, phenotype is also correlated with other behaviours, including: phagocytic ability (Schulz et al. 2019), lipid efflux to HDL (Lin et al. 2021) and migratory propensity (Cui et al. 2018). These effects could be incorporated by respectively allowing the rates of lipid uptake, k_{LDL} , k_r , k_{ap} , k_n , lipid efflux, k_H , and MDM egress, γ , to depend on ϕ .

Lipid-dependent MDM behaviours could also be included by allowing the corresponding rates to depend on ℓ . Lipid-dependent apoptosis, emigration and proliferation were analysed in the work of Watson et al. (2023), who found that such dependencies substantially altered total lesion lipid content, and the distribution of lipid amongst MDMs, apoptotic cells and the necrotic core. Importantly, some experimental studies indicate that lipid loading can inhibit macrophage pro-inflammatory responses (Leitinger and Schulman 2013; Kim et al. 2018). This effect could be accounted for in our model by allowing p_ϕ^+ to decrease with ℓ in reaction (5). Extending our model to account for phenotype and lipid-dependent rates produces coupling in the ODEs that would not admit a closed subsystem; analysis of these effects would rely heavily on numerical solutions.

Finally, we could extend the model to allow for spatial heterogeneity. Based on previous studies using spatially-resolved structured population models (Celora et al. 2023; Fiandaca et al. 2022; Pan 2022; Boulouz 2022; Hu 2019; Liu et al. 2015), we anticipate that analysis of a spatial extension would rely heavily on numerical simulations and bifurcation analysis.

In conclusion, in this paper we have presented a new mathematical model for early atherosclerosis in which the MDM population is structured according to phenotype and lipid content. The model indicates that lesion composition depends sensitively on the relative density of LDL lipid to HDL capacity in the blood, and the LDL retention capacity of the artery wall. Numerical and analytical results at steady state show that MDM phenotype and lipid content are monotonically correlated via a power law, the phenotype marginal distribution is unimodal, and the lipid content distribution may attain a unimodal, quasi-uniform or decreasing profile. These findings develop the current understanding of macrophage heterogeneity in early atherosclerosis.

Appendix A Parameter Estimation

The exchange rates, π_L^0 , π_L^1 , π_H^0 and π_H^1 are obtained by dividing the respective permeabilities by the human coronary artery tunica intima thickness (~ 0.24 mm (Holzapfel et al. 2005)). We note that the intimal thickness in mice is considerably smaller (~ 0.01 mm (Thon et al. 2018)), and so murine exchange rates are higher.

The maximum MDM entry rate, σ_M , is based on data from monocyte transmigration experiments (Williams et al. 2009). Specifically, Williams et al. observed that when human monocytes were placed above stimulated endothelial cells, approximately 20% entered the sub-endothelial layer within 1.5 hours. Multiplying this rate by 350 mm^{-3} ,

a typical blood monocyte density (Nelson 2014), gives 34000 mm^{-3} per month. Since approximately half the incoming monocytes do not differentiate into macrophages and leave the lesion within 48 hours (Lee et al. 2019), we estimate $\sigma_M = 17000 \text{ mm}^{-3}$ per month.

The uptake and efflux rates are obtained from *in vitro* experiments. We note that the free LDL uptake rate, k_{LDL} , is calibrated to data for native LDL (data for oxidised LDL yields a slightly higher but comparable estimate), while the larger rLDL uptake rate, k_r , is based on aggregated LDL data. This is reasonable since proteoglycan-bound LDL aggregates into lipid droplets that are more readily taken up by MDMs *in vivo* (Öörni and Kovanen 2021). The apoptotic lipid uptake rate, k_{ap} , has been scaled down from its *in vitro* estimate by a factor 19 to account for the 19-fold deficiency in efferocytosis measured in human atherosclerotic plaques (Schrijvers et al. 2005).

The mediator mass, Δs , and natural decay rate, δ_s , are based on data for the inflammatory mediator TNF, which has a molecular weight of 17kDa in its secreted form as a monomer and a 19 minute half-life (Atzeni and Sarzi-Puttini 2013; Liu et al. 2021). Other mediators have a comparable mass and half-life (e.g. 15 kDa and 20 min respectively for the resolving mediator IL-4 (Liu et al. 2021)).

We estimate the rate of rLDL-stimulated mediator production from resident cells, α , using reports that MDMs are observed in murine atherosclerotic lesions within 2 weeks of high fat diet treatment (Williams et al. 2020). The value $\alpha = 3.5 \times 10^{-3}$ per month ensures that the MDM density in our model is approximately 350 mm^{-3} (approximately blood monocyte concentration) in 2 weeks when $L^{(0)} = 750 \text{ mg/dL}$.

The MDM phenotypic plasticity, χ , is calibrated to experiments of macrophage phenotype modulation *in vitro* (Tarique et al. 2015). Tarique et al. observed that macrophages exposed to inflammatory and resolving mediators at 20 ng/mL underwent phenotypic polarisation in 2 days. We fix $\chi = 6.3 \times 10^{-4}$ so that phenotype modulation in our model occurs on this timescale (i.e. $\hat{\Phi}_M(t = 2\text{days}) = \pm 1/2$ if $S_{\pm} = 20\text{ng/mL}$ and $\hat{\Phi}_M(t = 0) = 0$).

Finally, we note that the lipid uptake/efflux increment, Δa , and maximal structure indices, ℓ_{\max} and ϕ_{\max} , are model abstractions. In reality, lipid increments vary substantially depending on the specific interaction. The smallest increment is likely that associated with efflux, given that each HDL particle can store approximately 75kDa of cholesterol. The largest increment is likely that due to apoptotic or necrotic lipid uptake, which we can assume to be smaller than the endogenous lipid content, a_0 , since cellular uptake *in vivo* is typically piecemeal rather than involving whole cell engulfment (Taefehshokr et al. 2021). We fix $\Delta a = 16\text{pg}$ as a reasonable intermediate value. This choice means that $\ell_{\max} = \kappa/\Delta a \approx 100$. The value of ϕ_{\max} has an upper bound of $(2\chi)^{-1} \approx 83000$ since the phenotype transition probabilities in Eq. (5) must satisfy $p_{\phi}^{\pm} \leq 1$. We fix $\phi_{\max} = 50$ so that phenotype and lipid content are equally resolved in our model.

Acknowledgements KLC acknowledges support from the Oxford Australia Scholarships Fund and Clarendon Scholars' Association. KLC and HMB would like to thank the Isaac Newton Institute for Mathematical Sciences, Cambridge, for support and hospitality during the programme Mathematics of movement: an interdisciplinary approach to mutual challenges in animal ecology and cell biology, where work on this paper was undertaken. This work was supported by EPSRC grant EP/R014604/1. All authors acknowl-

edge funding (to MRM, HMB) from the Australia Research Council Discovery Program, grant number DP200102071. We also wish to thank the anonymous reviewers for their constructive comments.

Declarations

Conflict of interest The authors declare that they have no conflict of interest.

Open Access This article is licensed under a Creative Commons Attribution 4.0 International License, which permits use, sharing, adaptation, distribution and reproduction in any medium or format, as long as you give appropriate credit to the original author(s) and the source, provide a link to the Creative Commons licence, and indicate if changes were made. The images or other third party material in this article are included in the article's Creative Commons licence, unless indicated otherwise in a credit line to the material. If material is not included in the article's Creative Commons licence and your intended use is not permitted by statutory regulation or exceeds the permitted use, you will need to obtain permission directly from the copyright holder. To view a copy of this licence, visit <http://creativecommons.org/licenses/by/4.0/>.

References

- Ahmed IU, Byrne HM, Myerscough MR (2023) Macrophage anti-inflammatory behaviour in a multi-phase model of atherosclerotic plaque development. *Bull Math Biol* 85(5):37. <https://doi.org/10.1007/s11538-023-01142-7>
- Allen RM, Michell DL, Cavnar AB, Zhu W, Makhijani N, Contreras DM, Raby CA, Semler EM, DeJulius C, Castleberry M et al (2022) LDL delivery of microbial small RNAs drives atherosclerosis through macrophage TLR8. *Nat Cell Biol* 24(12):1701–1713. <https://doi.org/10.1038/s41556-022-01030-7>
- Atzeni F, Sarzi-Puttini P (2013) Tumor necrosis factor. *Brenner's encyclopedia of genetics*, pp 229–231
- Avgerinos NA, Neofytou P (2019) Mathematical modelling and simulation of atherosclerosis formation and progress: a review. *Ann Biomed Eng* 47:1764–1785. <https://doi.org/10.1007/s10439-019-02268-3>
- Bäck M, Yurdagül A Jr, Tabas I, Öörni K, Kovanen PT (2019) Inflammation and its resolution in atherosclerosis: mediators and therapeutic opportunities. *Nat Rev Cardiol* 16(7):389–406. <https://doi.org/10.1038/s41569-019-0169-2>
- Bancells C, Benítez S, Jauhainen M, Ordóñez-Llanos J, Kovanen PT, Villegas S, Sánchez-Quesada JL, Katarina O et al (2009) High binding affinity of electronegative LDL to human aortic proteoglycans depends on its aggregation level. *J Lipid Res* 50(3):446–455. <https://doi.org/10.1194/jlr.M800318-JLR200>
- Barrett TJ (2020) Macrophages in atherosclerosis regression. *Arterioscler Thromb Vasc Biol* 40(1):20–33. <https://doi.org/10.1161/ATVBAHA.119.312802>
- Bayani A, Dunster JL, Crofts JJ, Nelson MR (2020) Spatial considerations in the resolution of inflammation: elucidating leukocyte interactions via an experimentally-calibrated agent-based model. *PLoS Comput Biol* 16(11):1008413. <https://doi.org/10.1371/journal.pcbi.1008413>
- Bernard S, Pujo-Menjouet L, Mackey MC (2003) Analysis of cell kinetics using a cell division marker: mathematical modeling of experimental data. *Biophys J* 84(5):3414–3424. [https://doi.org/10.1016/S0006-3495\(03\)70063-0](https://doi.org/10.1016/S0006-3495(03)70063-0)
- Bezyaev V, Sadekov N, Volpert V (2020) A model of chronic inflammation in atherosclerosis. *ITM Web Conf* 31:04002. <https://doi.org/10.1051/itmconf/20203104002>
- Boulouz A (2022) A spatially and size-structured population model with unbounded birth process. *Discr Contin Dyn Syst Ser B*. <https://doi.org/10.3934/dcdsb.2022038>
- Brouckaert G, Kalai M, Krysko DV, Saelens X, Vercammen D, Ndlovu M, Haegeman G, D'Herde K, Vandenaabeele P (2004) Phagocytosis of necrotic cells by macrophages is phosphatidylserine dependent and does not induce inflammatory cytokine production. *Mol Biol Cell* 15(3):1089–1100
- Brown BN, Valentin JE, Stewart-Akers AM, McCabe GP, Badylak SF (2009) Macrophage phenotype and remodeling outcomes in response to biologic scaffolds with and without a cellular component. *Biomaterials* 30(8):1482–1491. <https://doi.org/10.1016/j.biomaterials.2008.11.040>
- Bulezai MA, Dubbeldam JL (2012) Long time evolution of atherosclerotic plaques. *J Theor Biol* 297:1–10. <https://doi.org/10.1016/j.jtbi.2011.11.023>

- Cai Y, Li Z (2021) Mathematical modeling of plaque progression and associated microenvironment: How far from predicting the fate of atherosclerosis? *Comput Methods Programs Biomed* 211:106435. <https://doi.org/10.1016/j.cmpb.2021.106435>
- Calvez V, Ebde A, Meunier N, Raouf A (2009) Mathematical modelling of the atherosclerotic plaque formation. In: *ESAIM: Proceedings*, vol. 28, pp. 1–12. <https://doi.org/10.1051/proc/2009036>. EDP Sciences
- Celora GL, Byrne HM, Kevrekidis P (2023) Spatio-temporal modelling of phenotypic heterogeneity in tumour tissues and its impact on radiotherapy treatment. *J Theor Biol* 556:111248. <https://doi.org/10.1016/j.jtbi.2022.111248>
- Chalmers AD, Cohen A, Bursill CA, Myerscough MR (2015) Bifurcation and dynamics in a mathematical model of early atherosclerosis: How acute inflammation drives lesion development. *J Math Biol* 71:1451–1480. <https://doi.org/10.1007/s00285-015-0864-5>
- Chalmers AD, Bursill CA, Myerscough MR (2017) Nonlinear dynamics of early atherosclerotic plaque formation may determine the efficacy of high density lipoproteins (hdl) in plaque regression. *PLoS ONE* 12(11):0187674. <https://doi.org/10.1371/journal.pone.0187674>
- Chambers KL, Watson MG, Myerscough MR (2022) A lipid-structured mathematical model of atherosclerosis with macrophage proliferation. *arXiv preprint arXiv:2205.04715*. <https://doi.org/10.48550/arXiv.2205.04715>
- Chambers KL, Myerscough MR, Byrne HM (2023) A new lipid-structured model to investigate the opposing effects of LDL and HDL on atherosclerotic plaque macrophages. *Math Biosci*. <https://doi.org/10.1016/j.mbs.2023.108971>
- Chen C, Khismatullin DB (2015) Oxidized low-density lipoprotein contributes to atherogenesis via co-activation of macrophages and mast cells. *PLoS ONE* 10(3):0123088. <https://doi.org/10.1371/journal.pone.0123088>
- Cohen A, Myerscough MR, Thompson RS (2014) Athero-protective effects of high density lipoproteins (HDL): an ode model of the early stages of atherosclerosis. *Bull Math Biol* 76:1117–1142. <https://doi.org/10.1007/s11538-014-9948-4>
- Cooper G, Adams K (2022) *The cell: a molecular approach*. Oxford University Press, Oxford
- Corti A, Chiastra C, Colombo M, Garbey M, Migliavacca F, Casarin S (2020) A fully coupled computational fluid dynamics-agent-based model of atherosclerotic plaque development: multiscale modeling framework and parameter sensitivity analysis. *Comput Biol Med* 118:103623. <https://doi.org/10.1016/j.combiomed.2020.103623>
- Costopoulos C, Huang Y, Brown AJ, Calvert PA, Hoole SP, West NE, Gillard JH, Teng Z, Bennett MR (2017) Plaque rupture in coronary atherosclerosis is associated with increased plaque structural stress. *JACC Cardiovasc Imaging* 10(12):1472–1483. <https://doi.org/10.1016/j.jcmg.2017.04.017>
- Cui K, Ardell CL, Podolnikova NP, Yakubenko VP (2018) Distinct migratory properties of m1, m2, and resident macrophages are regulated by $\alpha\delta\beta 2$ and $\alpha m\beta 2$ integrin-mediated adhesion. *Front Immunol* 9:2650. <https://doi.org/10.3389/fimmu.2018.02650>
- Dalli J, Serhan CN (2012) Specific lipid mediator signatures of human phagocytes: microparticles stimulate macrophage efferocytosis and pro-resolving mediators. *Blood J Am Soc Hematol* 120(15):60–72. <https://doi.org/10.1182/blood-2012-04-423525>
- Daskalopoulos EP, Hermans KC, van Delft L, Altara R, Blankesteyn WM (2015) The role of inflammation in myocardial infarction. In: *Matthijs Blankesteyn W, Altara R (eds) Inflammation in heart failure*. Elsevier, Amsterdam
- Decker C, Sadhu S, Fredman G (2021) Pro-resolving ligands orchestrate phagocytosis. *Front Immunol* 12:660865. <https://doi.org/10.3389/fimmu.2021.660865>
- Dib L, Koneva LA, Edseldt A, Zurke Y-X, Sun J, Nitulescu M, Attar M, Lutgens E, Schmidt S, Lindholm MW et al (2023) Lipid-associated macrophages transition to an inflammatory state in human atherosclerosis, increasing the risk of cerebrovascular complications. *Nat Cardiovasc Res* 2(7):656–672. <https://doi.org/10.1038/s44161-023-00295-x>
- Doumic M (2007) Analysis of a population model structured by the cells molecular content. *Math Model Nat Phenom* 2(3):121–152. <https://doi.org/10.1051/mmnp:2007006>
- Fiandaca G, Bernardi S, Scianna M, Delitala ME (2022) A phenotype-structured model to reproduce the avascular growth of a tumor and its interaction with the surrounding environment. *J Theor Biol* 535:110980. <https://doi.org/10.1016/j.jtbi.2021.110980>
- Fok P-W (2012) Mathematical model of intimal thickening in atherosclerosis: vessel stenosis as a free boundary problem. *J Theor Biol* 314:23–33. <https://doi.org/10.1016/j.jtbi.2012.07.029>

- Fok P-W (2012) Growth of necrotic cores in atherosclerotic plaque. *Math Med Biol J IMA* 29(4):301–327. <https://doi.org/10.1093/imammb/dqr012>
- Fok P-W, Lanzer P (2018) Media sclerosis drives and localizes atherosclerosis in peripheral arteries. *PLoS ONE* 13(10):0205599. <https://doi.org/10.1371/journal.pone.0205599>
- Fok P-W, Mirzaei NM (2021) Modeling the Glagov's compensatory enlargement of human coronary atherosclerotic plaque. In: Ohayon J, Finet Gerard, Pettigrew RI (eds) *Biomechanics of coronary atherosclerotic plaque*. Elsevier, New York, pp 107–130. <https://doi.org/10.1016/B978-0-12-817195-0.00004-4>
- Ford HZ, Byrne HM, Myerscough MR (2019) A lipid-structured model for macrophage populations in atherosclerotic plaques. *J Theor Biol* 479:48–63. <https://doi.org/10.1016/j.jtbi.2019.07.003>
- Ford HZ, Zeboudj L, Purvis GS, Ten Bokum A, Zarebski AE, Bull JA, Byrne HM, Myerscough MR, Greaves DR (2019) Efferoctocytosis perpetuates substance accumulation inside macrophage populations. *Proc R Soc B* 286(1904):20190730. <https://doi.org/10.1098/rspb.2019.0730>
- Friedman A, Hao W (2015) A mathematical model of atherosclerosis with reverse cholesterol transport and associated risk factors. *Bull Math Biol* 77:758–781. <https://doi.org/10.1007/s11538-014-0010-3>
- Gonzalez L, Trigatti BL (2017) Macrophage apoptosis and necrotic core development in atherosclerosis: a rapidly advancing field with clinical relevance to imaging and therapy. *Can J Cardiol* 33(3):303–312. <https://doi.org/10.1016/j.cjca.2016.12.010>
- Guyton JR, Klemp KF (1989) The lipid-rich core region of human atherosclerotic fibrous. Plaques prevalence of small lipid droplets and vesicles by electron microscopy. *Am J Pathol* 134(3):705
- Guyton JR, Klemp KF (1996) Development of the lipid-rich core in human atherosclerosis. *Arterioscler Thromb Vasc Biol* 16(1):4–11. <https://doi.org/10.1161/01.atv.16.1.4>
- Hao W, Friedman A (2014) The LDL-HDL profile determines the risk of atherosclerosis: a mathematical model. *PLoS ONE* 9(3):90497. <https://doi.org/10.1371/journal.pone.0090497>
- Hodgkinson A, Le Cam L, Trucu D, Radulescu O (2019) Spatio-genetic and phenotypic modelling elucidates resistance and re-sensitisation to treatment in heterogeneous melanoma. *J Theor Biol* 466:84–105. <https://doi.org/10.1016/j.jtbi.2018.11.037>
- Holzappel GA, Sommer G, Gasser CT, Regitnig P (2005) Determination of layer-specific mechanical properties of human coronary arteries with nonatherosclerotic intimal thickening and related constitutive modeling. *Am J Physiol Heart Circ Physiol* 289(5):2048–2058. <https://doi.org/10.1152/ajpheart.00934.2004>
- Hu W (2019) Spatial-temporal patterns of a two age structured population model with spatial non-locality. *Comput Math Appl* 78(1):123–135. <https://doi.org/10.1016/j.camwa.2019.02.030>
- Insull W Jr (2009) The pathology of atherosclerosis: plaque development and plaque responses to medical treatment. *Am J Med* 122(1):3–14. <https://doi.org/10.1016/j.amjmed.2008.10.013>
- Islam MH, Johnston P (2015) A mathematical model for atherosclerotic plaque formation and arterial wall remodelling. *ANZIAM J* 57:320–345. <https://doi.org/10.21914/anziamj.v57i0.10386>
- Kadamoto S, Izumi K, Mizokami A (2021) Macrophage polarity and disease control. *Int J Mol Sci* 23(1):144. <https://doi.org/10.3390/ijms23010144>
- Kang H, Huo X, Ruan S (2020) Nonlinear physiologically structured population models with two internal variables. *J Nonlinear Sci* 30:2847–2884. <https://doi.org/10.1007/s00332-020-09638-5>
- Kim K, Shim D, Lee JS, Zaitsev K, Williams JW, Kim K-W, Jang M-Y, Seok Jang H, Yun TJ, Lee SH et al (2018) Transcriptome analysis reveals nonfoamy rather than foamy plaque macrophages are proinflammatory in atherosclerotic murine models. *Circ Res* 123(10):1127–1142. <https://doi.org/10.1161/CIRCRESAHA.118.312804>
- Kloc M, Usef A, Kubiak JZ, Ghobrial RM (2020) Role of macrophages and RhoA pathway in atherosclerosis. *Int J Mol Sci* 22(1):216. <https://doi.org/10.3390/ijms22010216>
- Kontush A, Therond P, Zerrad A, Couturier M, Nègre-Salvayre A, de Souza JA, Chantepie S, Chapman MJ (2007) Preferential sphingosine-1-phosphate enrichment and sphingomyelin depletion are key features of small dense hdl3 particles: relevance to antiapoptotic and antioxidative activities. *Arterioscler Thromb Vasc Biol* 27(8):1843–1849. <https://doi.org/10.1161/ATVBAHA.107.145672>
- Kritharides L, Christian A, Stoudt G, Morel D, Rothblat GH (1998) Cholesterol metabolism and efflux in human THP-1 macrophages. *Arterioscler Thromb Vasc Biol* 18(10):1589–1599. <https://doi.org/10.1161/01.ATV.18.10.1589>
- Laroche B, Perasso A (2016) Threshold behaviour of a SI epidemiological model with two structuring variables. *J Evol Equ* 16(2):293–315. <https://doi.org/10.1007/s00028-015-0303-5>

- Lee J-G, Koh SJ, Yoo SY, Yu JR, Lee SA, Koh G, Lee D (2012) Characteristics of subjects with very low serum low-density lipoprotein cholesterol and the risk for intracerebral hemorrhage. *Korean J Intern Med* 27(3):317. <https://doi.org/10.3904/kjim.2012.27.3.317>
- Lee SJ, Baek SE, Jang MA, Kim CD (2019) Sirt1 inhibits monocyte adhesion to the vascular endothelium by suppressing mac-1 expression on monocytes. *Exp Mol Med* 51(4):1–12. <https://doi.org/10.1038/s12276-019-0239-x>
- Leitinger N, Schulman IG (2013) Phenotypic polarization of macrophages in atherosclerosis. *Arterioscler Thromb Vasc Biol* 33(6):1120–1126. <https://doi.org/10.1161/ATVBAHA.112.300173>
- Lewis EA, Muñiz-Anquela R, Redondo-Angulo I, González-Cintado L, Labrador-Cantarero V, Bentzon JF (2023) Capacity for LDL (low-density lipoprotein) retention predicts the course of atherogenesis in the murine aortic arch. *Arterioscler Thromb Vasc Biol* 43(5):637–649. <https://doi.org/10.1161/ATVBAHA.122.318573>
- Lin P, Ji H-H, Li Y-J, Guo S-D (2021) Macrophage plasticity and atherosclerosis therapy. *Front Mol Biosci* 8:679797. <https://doi.org/10.3389/fmolb.2021.679797>
- Liu W, Yin Y, Zhou Z, He M, Dai Y (2014) OxLDL-induced IL-1 β secretion promoting foam cells formation was mainly via CD36 mediated ROS production leading to NLRP3 inflammasome activation. *Inflamm Res* 63:33–43. <https://doi.org/10.1007/s00011-013-0667-3>
- Liu Z, Tang H, Magal P (2015) Hopf bifurcation for a spatially and age structured population dynamics model. *Discr Cont Dyn Syst B* 20:1735–1757. <https://doi.org/10.3934/dcdsb.2015.20.1735>
- Liu C, Chu D, Kalantar-Zadeh K, George J, Young HA, Liu G (2021) Cytokines: from clinical significance to quantification. *Adv Sci* 8(15):2004433. <https://doi.org/10.1002/advs.202004433>
- Liu M, Cai Y, Pan J, Peter K, Li Z (2022) Macrophage polarization as a potential therapeutic target for atherosclerosis: a dynamic stochastic modelling study. *R Soc Open Sci* 9(8):220239. <https://doi.org/10.1098/rsos.220239>
- Liu M, Samant S, Vasa CH, Pedrigo RM, Oguz UM, Ryu S, Wei T, Anderson DR, Agrawal DK, Chatzizisis YS (2023) Co-culture models of endothelial cells, macrophages, and vascular smooth muscle cells for the study of the natural history of atherosclerosis. *PLoS ONE* 18(1):0280385. <https://doi.org/10.1371/journal.pone.0280385>
- Lui G, Myerscough MR (2021) Modelling preferential phagocytosis in atherosclerosis: delineating timescales in plaque development. *Bull Math Biol* 83(9):96. <https://doi.org/10.1007/s11538-021-00926-z>
- Madsen CM, Varbo A, Nordestgaard BG (2017) Extreme high high-density lipoprotein cholesterol is paradoxically associated with high mortality in men and women: two prospective cohort studies. *Eur Heart J* 38(32):2478–2486. <https://doi.org/10.1093/eurheartj/ehx163>
- Mc Auley MT (2022) Modeling cholesterol metabolism and atherosclerosis. *WIREs Mech Dis* 14(3):1546. <https://doi.org/10.1002/wsbm.1546>
- Meunier N, Muller N (2019) Mathematical study of an inflammatory model for atherosclerosis: a nonlinear renewal equation. *Acta Appl Math* 161:107–126. <https://doi.org/10.1007/s10440-018-0206-x>
- Mohammad Mirzaei N, Weintraub WS, Fok P-W (2020) An integrated approach to simulating the vulnerable atherosclerotic plaque. *Am J Physiol Heart Circ Physiol* 319(4):835–846. <https://doi.org/10.1152/ajpheart.00174.2020>
- Mukherjee D, Guin LN, Chakravarty S (2019) A reaction-diffusion mathematical model on mild atherosclerosis. *Model Earth Syst Environ* 5:1853–1865. <https://doi.org/10.1007/s40808-019-00643-6>
- Nelson DS (2014) Immunobiology of the macrophage. Academic Press, Cambridge
- Nielsen LB (1996) Transfer of low density lipoprotein into the arterial wall and risk of atherosclerosis. *Atherosclerosis* 123(1–2):1–15. [https://doi.org/10.1016/0021-9150\(96\)05802-9](https://doi.org/10.1016/0021-9150(96)05802-9)
- Niitsu Y, Watanabe N, Sone H, Neda H, Yamauchi N, Maeda M, Urushizaki I (1988) Analysis of the TNF receptor on KYM cells by binding assay and affinity cross-linking. *J Immunother* 7(3):276–282
- O'Carroll SJ, Kho DT, Wiltshire R, Nelson V, Rotimi O, Johnson R, Angel CE, Graham ES (2015) Pro-inflammatory $\text{tnf}\alpha$ and $\text{il-1}\beta$ differentially regulate the inflammatory phenotype of brain microvascular endothelial cells. *J Neuroinflamm* 12:1–18. <https://doi.org/10.1186/s12974-015-0346-0>
- Öörni K, Kovanen PT (2021) Aggregation susceptibility of low-density lipoproteins—a novel modifiable biomarker of cardiovascular risk. *J Clin Med* 10(8):1769. <https://doi.org/10.3390/jcm10081769>
- Orlova EV, Sherman MB, Chiu W, Mowri H, Smith LC, Gotto AM Jr (1999) Three-dimensional structure of low density lipoproteins by electron cryomicroscopy. *Proc Natl Acad Sci* 96(15):8420–8425. <https://doi.org/10.1073/pnas.96.15.8420>

- Pan Y (2022) Propagation dynamics for an age-structured population model in time-space periodic habitat. *J Math Biol* 84(3):19. <https://doi.org/10.1007/s00285-022-01721-7>
- Parton A, McGilligan V, O'Kane M, Baldrick FR, Watterson S (2016) Computational modelling of atherosclerosis. *Brief Bioinform* 17(4):562–575. <https://doi.org/10.1093/bib/bbv081>
- Penn MS, Saïdel GM, Chisolm GM (1994) Relative significance of endothelium and internal elastic lamina in regulating the entry of macromolecules into arteries in vivo. *Circ Res* 74(1):74–82. <https://doi.org/10.1161/01.res.74.1.74>
- Pérez S, Rius-Pérez S (2022) Macrophage polarization and reprogramming in acute inflammation: a redox perspective. *Antioxidants* 11(7):1394. <https://doi.org/10.3390/antiox11071394>
- Prosi M, Zunino P, Perktold K, Quarteroni A (2005) Mathematical and numerical models for transfer of low-density lipoproteins through the arterial walls: a new methodology for the model set up with applications to the study of disturbed lumenal flow. *J Biomech* 38(4):903–917. <https://doi.org/10.1016/j.jbiomech.2004.04.024>
- Pugin J, Schürer-Maly C, Leturcq D, Moriarty A, Ulevitch RJ, Tobias PS (1993) Lipopolysaccharide activation of human endothelial and epithelial cells is mediated by lipopolysaccharide-binding protein and soluble cd14. *Proc Natl Acad Sci* 90(7):2744–2748. <https://doi.org/10.1073/pnas.90.7.2744>
- Rothwell P (2007) Atherothrombosis and ischaemic stroke. *Br Med J*. <https://doi.org/10.1136/bmj.38964.489051.80>
- Sachet M, Liang YY, Oehler R (2017) The immune response to secondary necrotic cells. *Apoptosis* 22(10):1189–1204. <https://doi.org/10.1007/s10495-017-1413-z>
- Sanda GM, Stancu CS, Deleanu M, Toma L, Niculescu LS, Sima AV (2021) Aggregated LDL turn human macrophages into foam cells and induce mitochondrial dysfunction without triggering oxidative or endoplasmic reticulum stress. *PLoS ONE* 16(1):0245797. <https://doi.org/10.1371/journal.pone.0245797>
- Sansbury BE, Spite M (2016) Resolution of acute inflammation and the role of resolvins in immunity, thrombosis, and vascular biology. *Circ Res* 119(1):113–130. <https://doi.org/10.1161/CIRCRESAHA.116.307308>
- Saraste A, Pulkki K (2000) Morphologic and biochemical hallmarks of apoptosis. *Cardiovasc Res* 45(3):528–537. [https://doi.org/10.1016/S0008-6363\(99\)00384-3](https://doi.org/10.1016/S0008-6363(99)00384-3)
- Schoeneck M, Iggman D (2021) The effects of foods on LDL cholesterol levels: a systematic review of the accumulated evidence from systematic reviews and meta-analyses of randomized controlled trials. *Nutr Metab Cardiovasc Dis* 31(5):1325–1338. <https://doi.org/10.1016/j.numecd.2020.12.032>
- Schrijvers DM, De Meyer GR, Kockx MM, Herman AG, Martinet W (2005) Phagocytosis of apoptotic cells by macrophages is impaired in atherosclerosis. *Arterioscler Thromb Vasc Biol* 25(6):1256–1261. <https://doi.org/10.1161/01.ATV.0000166517.18801.a7>
- Schulz D, Severin Y, Zanotelli VRT, Bodenmiller B (2019) In-depth characterization of monocyte-derived macrophages using a mass cytometry-based phagocytosis assay. *Sci Rep* 9(1):1925. <https://doi.org/10.1038/s41598-018-38127-9>
- Schutte RJ, Parisi-Amon A, Reichert WM (2009) Cytokine profiling using monocytes/macrophages cultured on common biomaterials with a range of surface chemistries. *J Biomed Mater Res Part A* 88(1):128–139. <https://doi.org/10.1002/jbm.a.31863>
- Serhan CN, Levy BD et al (2018) Resolvins in inflammation: emergence of the pro-resolving superfamily of mediators. *J Clin Investig* 128(7):2657–2669. <https://doi.org/10.1172/JCI97943>
- Sha X, Meng S, Li X, Xi H, Maddaloni M, Pascual DW, Shan H, Jiang X, Wang H, Yang X-f (2015) Interleukin-35 inhibits endothelial cell activation by suppressing MAPK-AP-1 pathway. *J Biol Chem* 290(31):19307–19318. <https://doi.org/10.1074/jbc.M115.663286>
- Silva T, Jäger W, Neuss-Radu M, Sequeira A (2020) Modeling of the early stage of atherosclerosis with emphasis on the regulation of the endothelial permeability. *J Theor Biol* 496:110229. <https://doi.org/10.1016/j.jtbi.2020.110229>
- Smith EB, Staples EM (1982) Plasma protein concentrations in interstitial fluid from human aortas. *Proc R Soc London Ser B Biol Sci* 217(1206):59–75. <https://doi.org/10.1098/rspb.1982.0094>
- Sokol R, Wales J, Hudson G, Goldstein D, James N (1991) Changes in cellular dry mass during macrophage development. *Cells Tissues Organs* 142(3):246–248. <https://doi.org/10.1159/000147197>
- Stender S, Zilversmit D (1981) Transfer of plasma lipoprotein components and of plasma proteins into aortas of cholesterol-fed rabbits. Molecular size as a determinant of plasma lipoprotein influx. *Arteriosclerosis* 1(1):38–49. <https://doi.org/10.1161/01.atv.1.1.38>

- Tabas I, Bornfeldt KE (2016) Macrophage phenotype and function in different stages of atherosclerosis. *Circ Res* 118(4):653–667. <https://doi.org/10.1161/CIRCRESAHA.115.306256>
- Taefehshokh N, Yin C, Heit B (2021) Rab gtpases in the differential processing of phagocytosed pathogens versus efferocytosed apoptotic cells. <https://doi.org/10.14670/HH-18-252>
- Tarique AA, Logan J, Thomas E, Holt PG, Sly PD, Fantino E (2015) Phenotypic, functional, and plasticity features of classical and alternatively activated human macrophages. *Am J Respir Cell Mol Biol* 53(5):676–688. <https://doi.org/10.1165/rcmb.2015-00120C>
- Taruc K, Yin C, Wootton DG, Heit B (2018) Quantification of efferocytosis by single-cell fluorescence microscopy. *JVE*. <https://doi.org/10.3791/58149>
- Thon MP, Ford HZ, Gee MW, Myerscough MR (2018) A quantitative model of early atherosclerotic plaques parameterized using in vitro experiments. *Bull Math Biol* 80:175–214. <https://doi.org/10.1007/s11538-017-0367-1>
- Wang N, Liang H, Zen K (2014) Molecular mechanisms that influence the macrophage m1–m2 polarization balance. *Front Immunol* 5:614. <https://doi.org/10.3389/fimmu.2014.00614>
- Watanabe N, Kuriyama H, Sone H, Neda H, Yamauchi N, Maeda M, Niitsu Y (1988) Continuous internalization of tumor necrosis factor receptors in a human myosarcoma cell line. *J Biol Chem* 263(21):10262–10266
- Watson MG, Byrne HM, Macaskill C, Myerscough MR (2018) A two-phase model of early fibrous cap formation in atherosclerosis. *J Theor Biol* 456:123–136. <https://doi.org/10.1016/j.jtbi.2018.08.010>
- Watson MG, Byrne HM, Macaskill C, Myerscough MR (2020) A multiphase model of growth factor-regulated atherosclerotic cap formation. *J Math Biol* 81(2):725–767. <https://doi.org/10.1007/s00285-020-01526-6>
- Watson MG, Chambers KL, Myerscough MR (2023) A lipid-structured model of atherosclerotic plaque macrophages with lipid-dependent kinetics. *Bull Math Biol* 85(9):85. <https://doi.org/10.1007/s11538-023-01193-w>
- Wight TN (2018) A role for proteoglycans in vascular disease. *Matrix Biol* 71:396–420. <https://doi.org/10.1016/j.matbio.2018.02.019>
- Willemsen L, de Winther MP (2020) Macrophage subsets in atherosclerosis as defined by single-cell technologies. *J Pathol* 250(5):705–714. <https://doi.org/10.1002/path.5392>
- Williams KJ, Tabas I (2005) Lipoprotein retention and clues for atheroma regression. *Am Heart Assoc*. <https://doi.org/10.1161/01.ATV.0000174795.62387.d3>
- Williams MR, Sakurai Y, Zughair SM, Eskin SG, McIntire LV (2009) Transmigration across activated endothelium induces transcriptional changes, inhibits apoptosis, and decreases antimicrobial protein expression in human monocytes. *J Leukoc Biol* 86(6):1331–1343. <https://doi.org/10.1189/jlb.0209062>
- Williams JW, Martel C, Potteaux S, Esaulova E, Ingersoll MA, Elvington A, Saunders BT, Huang L-H, Habenicht AJ, Zinselmeyer BH et al (2018) Limited macrophage positional dynamics in progressing or regressing murine atherosclerotic plaques—brief report. *Arterioscler Thromb Vasc Biol* 38(8):1702–1710. <https://doi.org/10.1161/ATVBAHA.118.311319>
- Williams JW, Huang L-H, Randolph GJ (2019) Cytokine circuits in cardiovascular disease. *Immunity* 50(4):941–954. <https://doi.org/10.1016/j.immuni.2019.03.007>
- Williams JW, Zaitsev K, Kim K-W, Ivanov S, Saunders BT, Schrank PR, Kim K, Elvington A, Kim SH, Tucker CG et al (2020) Limited proliferation capacity of aortic intima resident macrophages requires monocyte recruitment for atherosclerotic plaque progression. *Nat Immunol* 21(10):1194–1204. <https://doi.org/10.1038/s41590-020-0768-4>
- Woudberg NJ, Pedretti S, Lecour S, Schulz R, Vuilleumier N, James RW, Frias MA (2018) Pharmacological intervention to modulate HDL: what do we target? *Front Pharmacol* 8:989. <https://doi.org/10.3389/fphar.2017.00989>
- Xie X (2022) Well-posedness of a mathematical model of diabetic atherosclerosis. *J Math Anal Appl* 505(2):125606. <https://doi.org/10.1016/j.jmaa.2021.125606>
- Yang N, Vafai K (2006) Modeling of low-density lipoprotein (LDL) transport in the artery—effects of hypertension. *Int J Heat Mass Transf* 49(5–6):850–867. <https://doi.org/10.1016/j.ijheatmasstransfer.2005.09.019>
- Yang N, Vafai K (2008) Low-density lipoprotein (LDL) transport in an artery—a simplified analytical solution. *Int J Heat Mass Transf* 51(3–4):497–505. <https://doi.org/10.1016/j.ijheatmasstransfer.2007.05.023>
- Yona S, Kim K-W, Wolf Y, Mildner A, Varol D, Breker M, Strauss-Ayali D, Viukov S, Guillemins M, Misharin A et al (2013) Fate mapping reveals origins and dynamics of monocytes and tissue macrophages under homeostasis. *Immunity* 38(1):79–91. <https://doi.org/10.1016/j.immuni.2012.12.001>

Yoneda S, Shibata S, Yamashita Y, Yanagishita M (2002) Biosynthesis of versican by rat dental pulp cells in culture. *Arch Oral Biol* 47(6):435–442. [https://doi.org/10.1016/s0003-9969\(02\)00029-8](https://doi.org/10.1016/s0003-9969(02)00029-8)

Publisher's Note Springer Nature remains neutral with regard to jurisdictional claims in published maps and institutional affiliations.